FIT Fukuoka Institute of Technology 福岡工業大学

GRADUATE SCHOOL OF ENGINEERING
FUKUOKA INSTITUTE OF TECHNOLOGY

Field Computation Time Reduction for Discrete Ray Tracing Method

by

Masafumi Takematsu

Adviser: Prof. Kazunori Uchida

2014

Contents

List of Figures

Acknowledgements

When I was a child, I used to be excited to build a crystal radio receiver, and I will never forget the clear sound the radio kit emitted for the first time. Since then, I have been interested in radio wave propagation: how radio waves go around and why unseen waves travel so far away.

Now, I run an information network design and consulting company, striving to construct mobile or radio networks as effectively as possible. From my experiences, I can tell how important it is to solve propagation related problems. And I am currently studying electromagnetic wave propagation in Fukuoka Institute of Technology(FIT), hoping that I can learn more about the characteristics of radio waves through the propagation analyzes. And it is a great honour for me to have an opportunity to conclude the research to the doctoral level.

Many useful suggestions and a great deal of collaboration with many different people helped me to complete this research. For this reason, there are some people that I would like to convey my gratitude from my heart.

First and foremost, I would like to express my deepest gratitude to my advisor Prof. Kazunori Uchida, for his orientation, support and guidance throughout the work.

I am greatly indebted to Prof. Leonard Barolli for his continuous support and help.

I would like to express special thanks to Prof. Hiroshi Maeda who encouraged me to tap into my scientific curiosity that has brought me to FIT by giving me an opportunity to study under Prof. Kazunori Uchida, with whom I have forged close bonds.

I am also grateful to Jiro Iwashige, Toshiaki Matsunaga, former Professors at FIT, Prof. Koki Watanabe and Prof. Takuya Semba for their kind help and support.

I would like to give special thanks to Dr. Junichi Honda of Electronic Navigation Research Institute for his kind help and continuous support.

I would like to thank Miss. Evjola Spaho, Mr. Yuki Kimura of NTT FIELD-TECHNO Corporation, Mr. Jun-Hyuck Lee, Mr. Keisuke Shigetomi, Mr. Takuma Hashimoto,

Mr. Naoto Hadano, Mr. Shinji Sakamoto and many other researchers and students who discussed various topics with me and kindly gave me many useful suggestions and advice.

I appreciate the help and support of the above-mentioned people, but of none more so than my wife and every other family members for their constant encouragement and love. This thesis would never have been possible without their continuous motivation, advice and support.

Abstract

Radio communication services have been widely expanding thanks to high-performing network systems. To design and construct these high-performance radio communication network systems, the estimation of electromagnetic fields, along with their various propagation environments, is very important. Particularly these days, analyzing the propagation characteristics of electromagnetic waves traveling along terrestrial surfaces is one of the most important issues for allocation of wireless base stations. It is well-known that multipath propagation over terrestrial surfaces and resulting time delay in the received signals cause some errors in a digital transmission system, thus its transmission quality could be deteriorated by the propagation environments.

To numerically analyze the characteristics of propagation along terrestrial surfaces, which are basically irregular and uneven and technically referred to as the Random Rough Surfaces (RRSs), the Discrete Ray Tracing Method (DRTM) was proposed by a research team led by Professor Kazunori Uchida at FIT in 2009. The essence of the DRTM is to discritize complicated terrestrial boundaries into piece-wise-linear profiles, which leads to such a ray searching algorithm that can reduce computation time. There are basically two advantages of the DRTM over other numerical methods: one is to compute electric field intensity in a relatively short time in comparison with the conventional Ray Tracing Method (RTM), and the other is to be able to treat large-scale RRSs.

Although the DRTM method enables us to analyze the propagation behaviors over various land surface structures, it still requires a certain period of time to compute in case a path is relatively long. To shorten computation time, we need to maximize discretization, but that may risk accuracy. Thus we have investigated the sampling rate of discretization in case of long distance propagation, with an eye to keeping the accuracy of both terrestrial surface profiling and electric field intensity. At present, as there is no appropriate guideline available for how we should discretize terrestrial boundaries to achieve as few errors as possible, we need to find and define a way we should discretize those boundaries.

The author proposes a modified DRTM which reduces computation time from the viewpoints of ray searching and field computation, by using the inner products of vectors to change the lengths of discretized plates in accordance with the RRSs. In other words, the proposed modified DRTM takes into consideration variable plate lengths for various shapes of the surfaces of any given terrain: for example, a short-plate length for a mountain summit and a long length for level ground and the other. To make field computation accurate and faster, the author employs an algorithm modified from that of the above-mentioned DRTM and an approximation of the Fresnel function. The numerical results listed in Chapter 7 show that the modified algorithm has a good behavior for reducing computation time and keeping accurate field computation.

The contributions of our research work are as follows.

- Evaluation of the DRTM comparing with the results of rigorous solutions.
- Application of the DRTM to long distance propagation.
- Proposal of the modified algorithm for discretizing RRSs.
- Implementation and evaluation of the modified algorithm.

The thesis is organized as follows. Chapter 1 describes the background, purpose and contributions of the study. Chapter 2 reviews the principles of DRTM. Chapter 3 evaluates the DRTM to check its accuracy. Chapter 4 explains the application of the DRTM to a long distance. Chapter 5 discusses diffracted edge points and their sampling rates. Chapter 6 presents the modified algorithm for RRS discretization. Chapter 7 shows some numerical results of the modified algorithm. Chapter 8 presents the conclusions of the research and its future work.

Chapter 1

Introduction

1.1 Background

Since Guglielmo Marconi first demonstrated radio's ability to provide continuous contact with ships sailing the English Channel in 1897, the ability to communicate with people on the move has evolved remarkably. And since then, new wireless communication methods and services have been extensively adopted by people throughout the world. In the meantime, to meet increasing demand for new services, radio industries have been required to construct effective radio communication facilities [1]. Japan in particular, following the U.S and Europe since the end of the second World War, has been constructing communication and broadcasting radio networks throughout the country. However, because of mountainous regions covering much of the country, Japanese industries and researchers have had to work hard to solve the problems related to radio wave propagation.

In March 2011, the Great East Japan Earthquake and unprecedented tsunami devastated northern Japan. Many lives were fortunately saved by tsunami warnings issued in advance. Based on this experience, the Japanese government is now promoting the development and enhancement of a disaster-prevention communication network across the nation. The network is to secure communications and to collect and disseminate information promptly and steadily in the event of a disaster [2]. The government as well as many Japanese have reconfirmed that other highly-developed communication networks, such as mobile communication network systems and digital TV broadcasting system must also remain stable in emergency [3].

To design and construct these high-performance radio communication network systems, the estimation of electromagnetic fields, along with their various environments, is

ever more important today to allocate wireless base stations effectively. And also important is the analysis of the propagation characteristics of the waves traveling along terrestrial surfaces. It is well-known that multi-path propagation over terrestrial surfaces cause incomplete communication due to diffused reflections. And this often results in time delay in the received signals, causing some errors in a digital transmission system [4, 5]. Thus the quality of communication could be deteriorated by multi-path propagation.

The propagation environments include open areas such as an urban or suburban topography and closed regions such as an office room or underground space. Whether open or closed, the sizes of scattering obstacles and the distances of electromagnetic (EM) wave propagation are generally larger and longer than the wavelengths of radio waves. Also, structures of the environments with many scattering obstacles are usually too complicated to be dealt with rigorously. As a result, it is necessary to apply an approximate numerical method, for example, the Finite Volume Time Domain (FVTD) method [6], [7], to such complicated diffraction problems.

As for the FVTD, it is common knowledge that the method is useful for arbitrarily treating profiled boundaries but it is rather useless for dealing with a long distance propagation as the method consumes a large amount of computer memory [9]. The DRTM was proposed in 2009 to numerically analyze the propagation characteristics along RRSs, the Random Rough Surfaces[10, 11]. There are some other numerical methods to analyze electromagnetic fields along the RRSs [12]-[20]. However, the DRTM has two advantages over the other numerical methods: one is to compute EM field intensity in a relatively short time, and the other is to treat large scale RRSs because the general Ray Tracing Method (RTM) is based on the Physical Optics and Geometrical Optics(PO/GO).

The DRTM enables us to save computation time of EM field intensity more efficiently as opposed to the conventional RTM. In short, the efficiency of the DRTM comes from by firstly searching rays between the source and the receiver, and secondly computing EM fields based on the traced rays. The DRTM can discretize not only the RRSs but also a ray tracing procedure, which results in saving time in ray searching [10, 11]. Among various options, the DRTM is a logical choice and used in this study. The author's team looks into the relationship between the field attenuation and the shapes of RRSs described as a correlation length (cl) and a height deviation (dv) [8]. The study also examines radio communication distances along RRSs [10, 11] and the importance of relay stations for the digital broadcasting services [3].

As has been discussed, the DRTM is one of the most suitable numerical techniques for analyzing electromagnetic fields in complicated natural environments, and it seems to be a good numerical method for treating propagation problems with a long communication distance [11]. Moreover, we have made clear the relationship between observational plate lengths and edge points which give rise to diffraction. The resolution is very useful for the DRTM to solve the propagation problems more accurately. The essence of the DRTM is to discretize complicated terrestrial boundaries into piece-wise-linear profiles, which results in computation-time reduction for ray searching.

Although the method enables us to analyze the propagation characteristics along land surface structures, including terrain profiles like a desert or mountain area, it still requires a certain period of time to compute in case of a long path. To shorten computation time, we need to maximize discretization, but that may run the risk of compromising accuracy. Thus we have investigated the sampling rates of discretization in case of long-distance propagation, with an eye to keeping the accuracy of both terrestrial surface profiling and EM field intensity. In the DRTM algorithm, a piece-wise-linear plate should be as small as possible to maintain RRS's real shapes, but at the same time each plate must be larger than a radio wavelength from a numerical reason based on the optical approximation.

Since the DRTM equally spaces sampling point for discretization, the plate length of which is constant, much ray searching time is required in case of long paths or 2D RRSs. To overcome this problem, we need a new method which can save more computation time, while maintaining correct RRS profiles and keeping numerical accuracy for field intensity. At present, as we have no appropriate guideline available for how we should discretize terrestrial boundaries to achieve as few errors as possible, we need to come up with our own yardstick to introduce a new method with accuracy. In this thesis, the author firstly reviews the principles of the DRTM, and secondly uses a cylindrical conductor to evaluate the DRTM when applied to EM-wave scattering. The accuracy of the DRTM is checked by comparing its results with rigorous analytical solutions.

The DRTM is also applied to plane wave diffraction by a conducting half-plane. Scattered fields for this type of problem can be computed rigorously by using the Fresnel function. The purpose of this evaluation is to analyze propagation characteristics in case of a long distance by actually incorporating real surface structures from the Geographic Information System (GIS) [3]. The author's team confirms that the DRTM is a useful numerical method to estimate a long distance propagation characteristics. We are aware that discretized analytical edge points should coincide with the summit points of an orig-

inal terrain profile, and intense sampling points are needed at the summits to accurately estimate the field intensity of shadow areas beyond the summits [21].

The author of this thesis proposes a modified DRTM which reduces computation time from the viewpoints of ray searching and field computation. The first step is to change the length of discretized plates of the RRSs by using the inner products of vectors related to those discretized plates. In other words, variable plate lengths for various shapes of land surfaces are taken into consideration; for example, a short length for a mountain summit and a long length for level ground and the other. To make field computation accurate and faster, the author employs a modified algorithm and an approximation of the Fresnel function. And the final step is to demonstrate the rates of time reduction in light of ray searching and field computation, and to discuss the effectiveness of the proposed method of this thesis. Its numerical results show that the proposed algorithm has a good behavior.

1.2 Thesis Purpose and Contribution

This thesis studies the DRTM as an effective method and evaluates it by comparing its performance results with rigorous solutions. To compute long-distance propagation, earth-profile data from the GIS is used. The author proposes the modified algorithm mentioned above to discrete RRSs efficiently and uses the algorithm to implement the method even more effectively. The thesis evaluates the new algorithm from its numerical results and discusses the effectiveness of the proposed, modified method.

At the present time, the DRTM still requires some time to analyze long-path propagation. To address this issue, the author's team looked for and have come to a solution to define how we should discrete terrestrial boundaries. The purpose of this paper is to present the modified algorithm to reduce computation time, while keeping the accuracy of RRS profiles and field intensity. To the best of our knowledge, there is not yet any case of real simulation architectures where an algorithm based on the same idea and serving the same purpose as this thesis has been implemented.

Our contributions are summarized as follows:

- Evaluation of the DRTM comparing with the results of rigorous solutions.
- Application of the DRTM to long distance propagation.
- Proposal of the modified algorithm for discretizing RRSs.

- Implementation and evaluation of the modified algorithm.

1.3 Thesis Outline

This thesis is organized into eight chapters and its structure is given in Fig. 1.1.

Chapter 1 serves as an introduction to the thesis, describing the background, purpose and contributions of the research and its outline.

Chapter 2 reviews the principles of the DRTM and introduces field computation to describe its theory, the discretization of rough surfaces, and ray tracing.

In **Chapter 3,** the author evaluates the DRTM to check its accuracy. As rigorous solutions are available to solve propagation problems caused by a cylinder, the author compares the results of the DRTM to the rigorous solutions by using scattered waves from the cylinder. In this chapter, the accuracy of the DRTM is discussed focussing on the number of plates discretizing the cylinder's surfaces.

Chapter 4 discusses related work on field estimation for long distance propagation problems. The application of the DRTM to a long distance and its results are described in this chapter.

Chapter 5 introduces diffracted edge points and their sampling rates. It explains that intense sampling rates are needed in the edge points and fewer sampling rates in plain areas.

In **Chapter 6** is presented the author's proposal of a modified algorithm. The chapter describes the reduction of computation time for ray searching by varying plate lengths in accordance with various shapes of land profiles.

In **Chapter 7**, the author discusses numerical results of the modified algorithm and evaluates the new method.

Chapter 8 concludes the thesis and discusses the future work of this research.

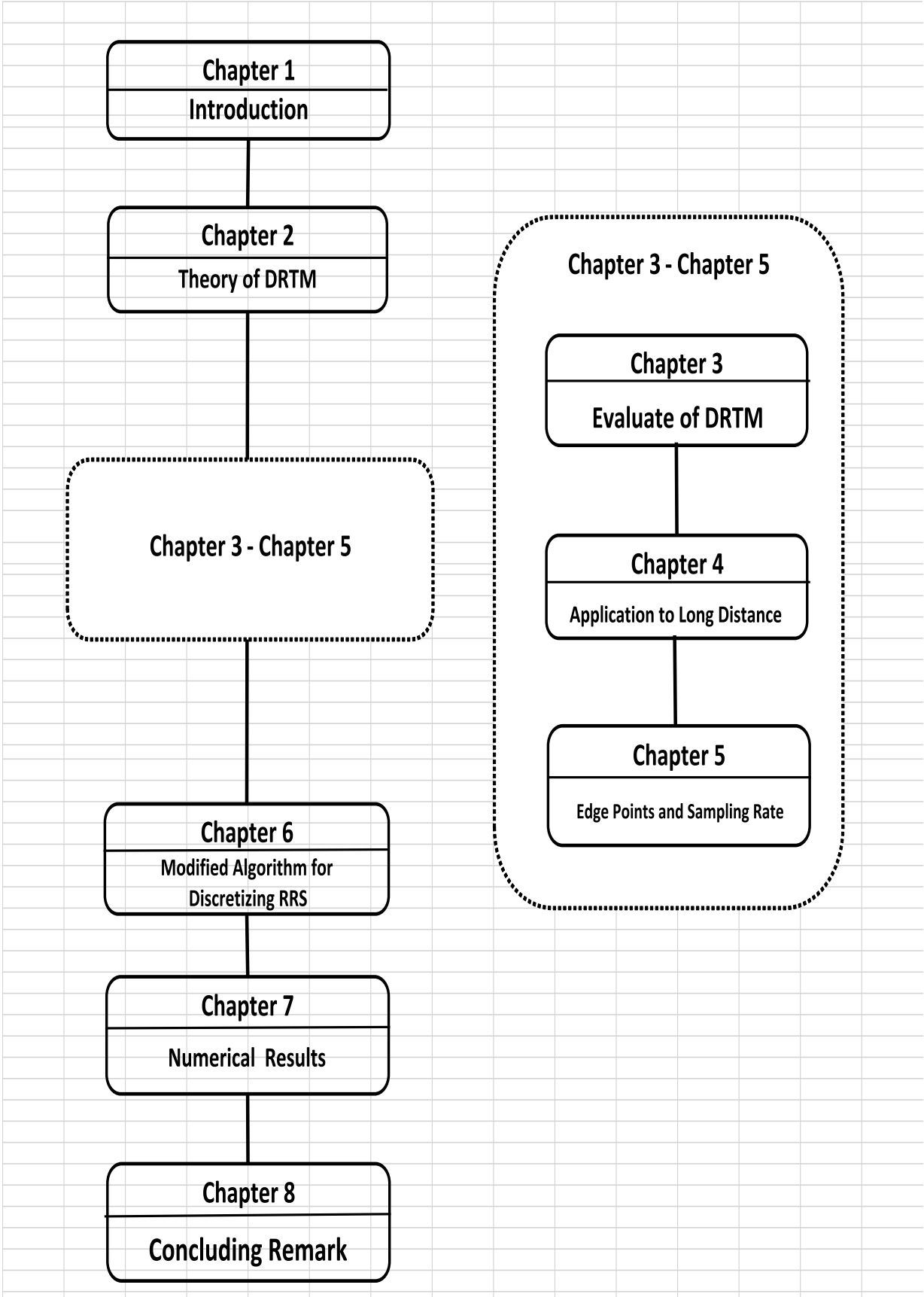

Figure 1.1: Thesis Structure.

Chapter 2

Theory of Discrete Ray Tracing Method

2.1 Introduction

The DRTM was proposed to numerically compute electromagnetic fields above the complicated terrestrial surfaces, such as desert, hilly terrain, vegetable field, sea surface and so on [10, 11]. These terrestrial surfaces are called random rough surfaces characterized by a correlation length (cl) and a height deviation (dv). To numerically analyze and simulate radio wave propagation characteristic along RRSs, we need various kinds of RRSs. In this chapter, we generate the RRSs by using the convolution method for only Gaussian type of spectrum.

2.2 Convolution Method

Starting from the method of direct RRS generation based on direct Fourier transformation method (DFT) [12], we have devised the convolution method for generating continuous RRS with arbitrary length [13]. Modifying and improving this convolution method, we have recently introduced the analytically expressed convolution method which can be applied to generate arbitrarily inhomogeneous RRS [14]. In this chapter, we firstly discuss convolution method focusing on 1D and 2D RRSs with Gaussian type of spectrum and generation by the method.

2.2.1 Gaussian types of 1D and 2D RRSs

Denote the spacial wave number by k for the Gaussian type of 1D RRS. Then its power spectrum and correlation function are given by

$$\begin{aligned} W(k) &= \frac{cldv}{2\sqrt{\pi}} \exp\left[-\left(\frac{kcl}{2}\right)^2\right] \\ \rho(x) &= dv \exp\left[-\left(\frac{x}{cl}\right)^2\right] \end{aligned} \tag{2.1}$$

where dv is the height standard deviation of RRS and cl is its correlation length. It should be noted that the correlation function $\rho(x)$ is computed by the Fourier transformation of the power spectrum $W(k)$ in Eq.(2.1). In this 1D case, amplitude spectrum $H(k)$ and its Fourier transform or amplitude weight function $h(x)$ are computed as follows:

$$\begin{aligned} H(k) &= dv \frac{\sqrt{cl}}{\sqrt{2\sqrt{\pi}}} \exp\left[-\left(\frac{kcl}{2\sqrt{2}}\right)^2\right] \\ h(x) &= 2dv \sqrt{\frac{\sqrt{\pi}}{cl}} \exp\left[-2\left(\frac{x}{cl}\right)^2\right] . \end{aligned} \tag{2.2}$$

Next we consider the Gaussian type of 2D RRS. We denote the spacial wave number vector by $\mathbf{k} = (k_x, k_y)$ with its amplitude $k = |\mathbf{k}|$ and the position vector by $\mathbf{r} = (x, y)$ with its amplitude $r = |\mathbf{r}|$. Then its power spectrum $W(\mathbf{k})$ and correlation function $\rho(\mathbf{r})$ are described as follows:

$$\begin{aligned} W(\mathbf{k}) &= \frac{cl^2 dv^2}{4\pi} \exp\left[-\left(\frac{kcl}{2}\right)^2\right] \\ \rho(\mathbf{r}) &= dv^2 \exp\left[-\left(\frac{r}{cl}\right)^2\right] . \end{aligned} \tag{2.3}$$

Of course, the Fourier transform of power spectrum $W(\mathbf{k})$ yields the correlation function $\rho(\mathbf{r})$ in Eq.(2.3). In this 2D case, amplitude spectrum $H(\mathbf{k})$ and its Fourier transform or amplitude weight function $h(\mathbf{r})$ are computed as follows:

$$\begin{aligned} H(\mathbf{k}) &= \frac{cldv}{2\sqrt{\pi}} \exp\left[-\left(\frac{kcl}{2\sqrt{2}}\right)^2\right] \\ h(\mathbf{r}) &= \frac{4\sqrt{\pi}dv}{cl} \exp\left[-2\left(\frac{r}{cl}\right)^2\right] . \end{aligned} \tag{2.4}$$

As shown in Eqs.(2.2) and (2.4), we have introduced the amplitude weighting functions $h(x)$ and $h(\mathbf{r})$ for the 1D and 2D Gaussian types of spectra, respectively. Since

these amplitude weighting functions are expressed in analytical forms, they can be easily discretized as follows:

$$\begin{aligned} \tilde{h}_m &\simeq \frac{\sqrt{\Delta x}}{\sqrt{2\pi}} h(m\Delta x) \\ \tilde{h}_{mn} &\simeq \frac{\sqrt{\Delta x \Delta y}}{2\pi} h(m\Delta x, n\Delta y) \end{aligned} \tag{2.5}$$

where $m, n = 0, \pm 1, \pm 2, \cdots$. It is worth noting that the discretizing intervals Δx and Δy must be dependent on RRS parameters dv and cl. In the subsequent section we will discuss the criterion for these discretizing intervals focusing on Gaussian type of RRSs.

2.2.2 RRS generation by convolution method

The final expression for 1D RRS generation based on the convolution method is summarized as follows:

$$f_m = \sum_{\mu=-M}^{M} \tilde{h}_\mu g_{m+\mu} \tag{2.6}$$

where f_m correspond to the profile of generated 1D RRS in an discrete form. Moreover, $\tilde{h}_\mu$ are the discretized weight functions given by Eq.(2.5) and g_m are the 1D series of the Gaussian random numbers with zero mean and unit deviation, that is

$$g_m \in N(0,1) \tag{2.7}$$

where $N(0,1)$ indicates the set of random variables in the normal distribution.

On the other hand, the final expression for 2D RRS generation based on the convolution method is summarized as follows:

$$f_{mn} = \sum_{\mu=-M}^{M} \sum_{\nu=-N}^{N} \tilde{h}_{\mu\nu} g_{m+\mu\ n+\nu} \tag{2.8}$$

where f_{mn} denote the profile of generated 2D RRS in a discrete form. Moreover, $\tilde{h}_{\mu\nu}$ are the discretized 2D weighting functions given by Eq.(2.5) and g_{mn} are the 2D series of the Gaussian random numbers with zero mean and unit deviation, that is

$$g_{mn} \in N(0,1) \tag{2.9}$$

where $N(0,1)$ indicates the normal distribution.

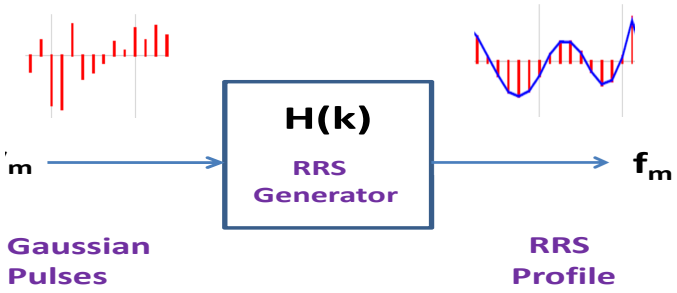

Figure 2.1: Diagram for the 1D RRS generator based on convolution method.

As long as the computational procedure of 1D RRS generation is concerned, its mechanism resembles the linear system governed by the convolution algorithm. Thus the numerical procedures are well demonstrated by the schematic picture as shown in Fig.2.1; the inputs are Gaussian impulse series, the impulse response function is the amplitude weighting function and the responses are the profile series of a generated RRS.

More importantly, the present analytical type of convolution method can treat inhomogeneous RRS by the following procedure. The discretized series of the amplitude weight functions in Eq.(2.5) include dv and cl as shown in Eqs.(2.2) and (2.4). The values of these two parameters are not necessarily constant but they can be changed arbitrarily from place to place. Thus, we can generate an inhomogeneous RRS which exhibits different statistical properties from one area to another.

Figures 2.2 and 2.3 show examples of RRS. We have selected following parameters: $cl = 30.0[m]$ and $dv = 5.0[m]$ in Fig.2.2, and $cl = 50.0[m]$ and $dv = 5.0[m]$ in Fig.2.3. It is shown that the larger cl is, the smoother RRS profile becomes.

2.3 Discretization of Rough Surface

The first step of the DRTM procedure is to discretize a 1D rough surface in terms of combination of straight lines so that it could be approximated by a piece wise linear line [10, 11]. It is important for this approximation that the computer memory should be as small as possible, for this reason, we propose the following discretization method. First,

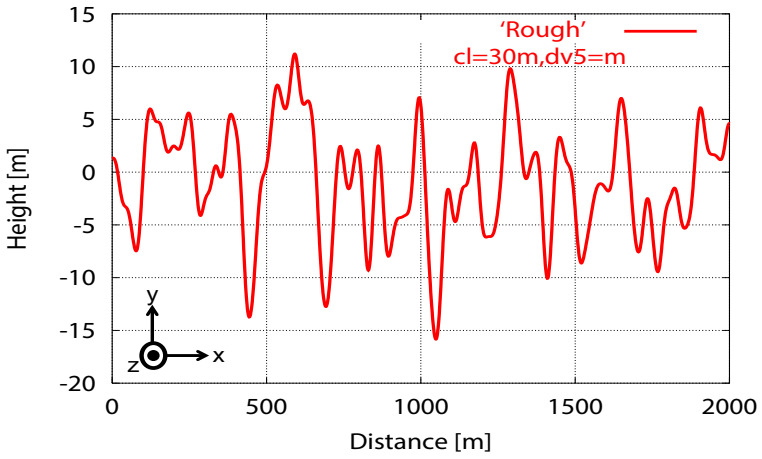

Figure 2.2: Examples of Gaussian random rough surface (cl=30m, dv=5m).

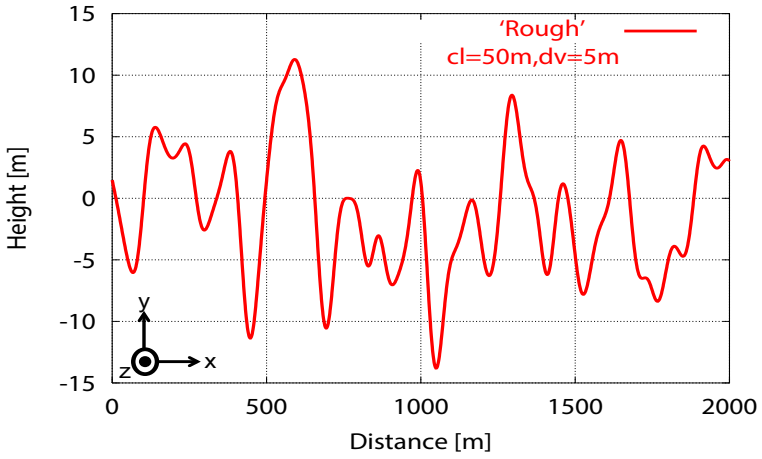

Figure 2.3: Examples of Gaussian random rough surface (cl=50m, dv=5m).

we divide x-axis into n_x straight lines with length D_x. Then we can discretize any types of rough surfaces in terms of representative points as follows:

$$\begin{aligned} &\rho_i = (x_i, H(x_i)) \\ &(i = 0, 1, 2, \cdots, n_x) \end{aligned} \tag{2.10}$$

where

$$x_i = D_x i \quad (i = 0, 1, 2, \cdots, n_x) \tag{2.11}$$

and $H(x)$ is the height function of 1D RRS, and D_x is the length of each straight line in the x-direction. In this chapter, we assume that the length of D_x is constant and defined by the discretized plate length.

Next we derive the normal vectors of the discretized straight lines as follows:

$$\begin{aligned} n_i &= (u_z \times a_i)/|u_z \times a_i| \\ &(i = 0, 1, 2, \cdots, n_x - 1) \end{aligned} \tag{2.12}$$

where u_z is the unit vector in z-direction, and the vector expression of the adjacent plates is given by

$$a_i = (\rho_{i+1} - \rho_i) \ . \tag{2.13}$$

It should be noted that only the position vectors ρ_i and the normal vectors n_i are enough to search rays for the 1D discretized RRS.

2.4 Discretization of Ray Tracing

In the present DRTM simulations, we have chosen the representative point of a straight line to be the starting point of the line, that is, at ρ_i in Eq.(2.10). We assume that arbitrary two plates of discretized RRS are in line of sight (LOS), if each representative point of straight line is in LOS. Otherwise, they are not in line of sight (NLOS) [10, 11].

Now, we divide rays into incident (source), source diffraction and image diffraction rays [10, 11]. The source diffraction is the diffraction of the incident wave or source wave, and it is classified into two types; one is a source diffraction in the illuminated region if the representative point of a straight line is in LOS, and the other is a source diffraction in the shadow region if it is in NLOS. We consider only the source diffraction rays with the shortest path from source to receiver. Thus the source diffraction rays are constructed so that the representative points in LOS or NLOS may form the shortest path from the source to the receiver.

On the other hand, we can construct image diffraction rays by connecting different two lines using representative points successively, if they are in LOS. It should be noted that the conventional reflection rays are included in the present image diffraction rays as a special case of rays which satisfy the Snell's law or the relationship that the incident and reflection angles are equal each other.

Let us explain the example of searched ray shown in Fig.2.4. First, we find the straight line from (5) to (8) which are in LOS. Second, we add the lines from S to (5) and from (8) to R, since S and (5) as well as (8) and R are in LOS. Thus, we obtain an approximate discrete ray from S to R through (5) and (8) as shown in black lines.

In order to obtain a more accurate ray, we can modify the discrete ray based on the imaging method. S_{i1} is an image source for first reflection point of line (5), and S_{i2} is an image point of first reflection point for second reflection point of line (8). The final ray plotted in arrow line shows that the ray emitted from S is first diffracted at the right edge of line at (5) and next reflected by line (8), and finally it reaches R. We call this type of diffraction as an image diffraction, since it is associated with reflection and the reflection might be described as an emission from the image point with respect to the related line.

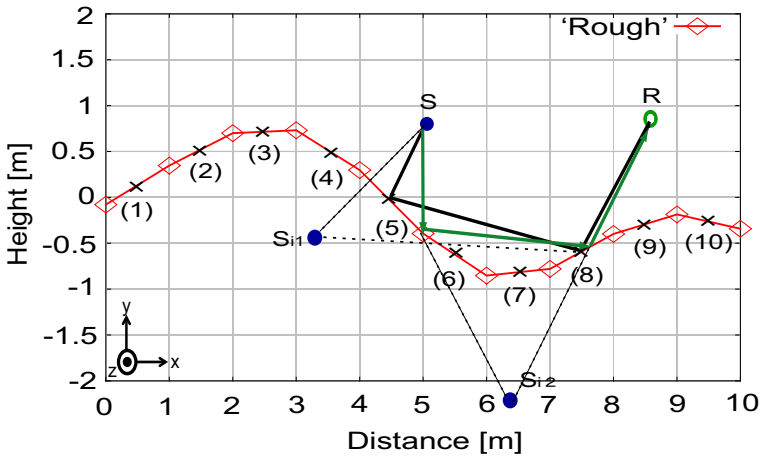

Figure 2.4: Example of searching the ray in case of LOS.

Let us explain another example of searched ray in Fig.2.5. First, we find a shortest path from (2) to (4) which are in NLOS and we also find a straight line (4) to (8) which are in LOS. Moreover, we add the straight line from S to (2) which are in LOS as well as the straight line from (8) to R which are also in LOS. Thus, we can draw an approximate discrete ray from S to R through (2), (3), (4) and (8). The discrete ray is shown by black lines.

In order to construct a more accurate ray, we modify the discrete ray so that the distance from S to (8) may be minimum, and we apply the imaging method to the discrete ray from(4) to R through (8). The final modified ray is plotted in arrow lines in Fig.2.5. The ray from S to (8) constitutes a diffraction. We call it a source diffraction, because it is

associated with shadowing of the incident wave from source S through line (3). The ray from edge (3) to R through (8) is included into image diffraction.

We need to consider not only source diffraction but also image diffraction in order to genellary analyze scattered waves from an obstacle. However, in this analysis, we assume that the ray is constituted as image diffraction when it is in LOS, on the other hand, the ray is constituted as source diffraction in case of NLOS.

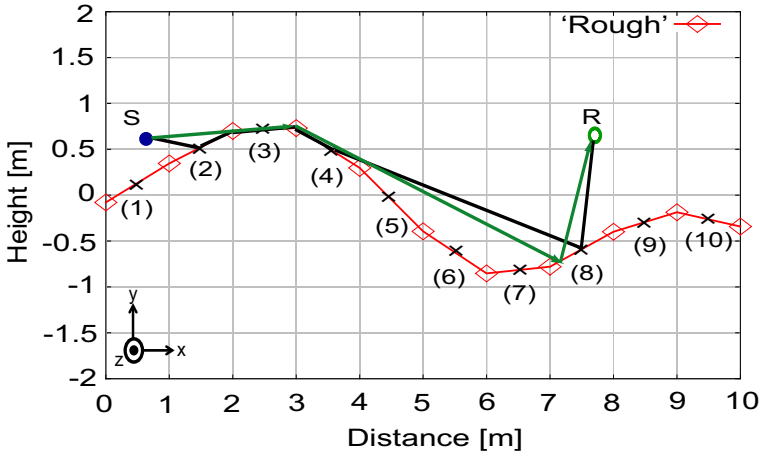

Figure 2.5: Example of searching the ray in case of NLOS.

Figure 2.6 shows a numerical example of traced rays. The source is placed at $x = 0[m]$ and $0.5[m]$ high above the rough surface, and the receiver is settled at $x = 1,380[m]$ and $0.5[m]$ high above the rough surface. In this numerical example, we have considered the rays up to the second order of reflections and diffractions, that is, incident, one-time reflection, two-time reflections and diffraction.

2.5 Field Computation

2.5.1 Incident and Reflected waves

Neglecting near fields, the electric field radiated from a small dipole antenna with input power P_i is expressed in the following vector form [22]:

$$\mathbf{E_0} = \sqrt{30GP_i}[(\mathbf{u_r} \times \mathbf{p}) \times \mathbf{u_r}]\Psi(r) \tag{2.14}$$

where $\mathbf{r}$ is a position vector from the source to a receiver and $r = |\mathbf{r}|$. The direction of the unit vector $\mathbf{u_r} = \mathbf{r}/r$ is from the source to the receiver, and $|\mathbf{u_r} \times \mathbf{p}| = D(\phi) = \sin\phi$

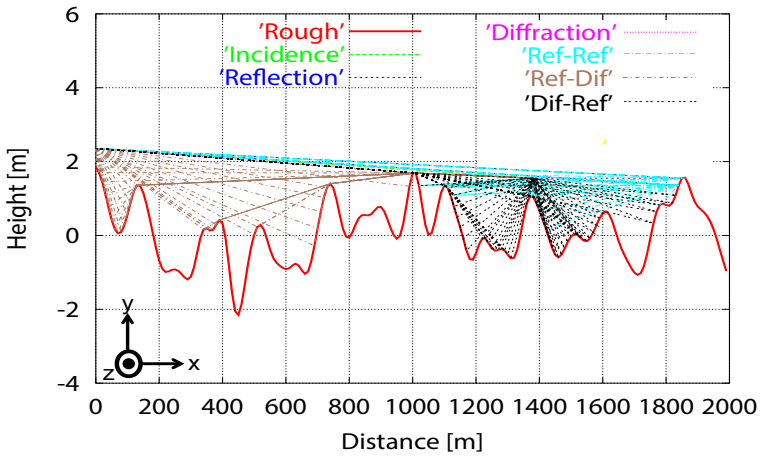

Figure 2.6: Examples of traced rays up to second scattered waves.

is the directivity of the small dipole antenna. The unit vector **p** is the direction of source antenna, and the source antenna gain is G. Moreover, the wave function is defined by

$$\Psi(r) = \frac{e^{-j\kappa r}}{r}, \qquad \kappa = \omega\sqrt{\varepsilon_0\mu_0} \tag{2.15}$$

where κ is the wave number in the free space, and the time dependence $e^{j\omega t}$ is assumed.

Figure 2.7 shows incident and reflected waves at a ground plane. We describe the incident wave as a source field since the wave radiates from a source, and we express the reflected wave as an image field since the wave behaves just as if it radiates from the image of the source. Received fields are expressed for E-wave and H-wave as follows:

$$\begin{aligned} E_z &= \Psi(r_0) + R^h(\theta)\Psi(r) \\ H_z &= \Psi(r_0) + R^v(\theta)\Psi(r) \end{aligned} \tag{2.16}$$

where θ is an incident angle and $r = r_1 + r_2$. The reflection coefficients for horizontal and vertical polarizations are given by [22]

$$\begin{aligned} R^h(\theta) &= \frac{\cos\theta - \sqrt{\varepsilon_c - \sin^2\theta}}{\cos\theta + \sqrt{\varepsilon_c - \sin^2\theta}} \\ R^v(\theta) &= \frac{\varepsilon_c\cos\theta - \sqrt{\varepsilon_c - \sin^2\theta}}{\varepsilon_c\cos\theta + \sqrt{\varepsilon_c - \sin^2\theta}} \\ \varepsilon_c &= \varepsilon_r - j\frac{\sigma}{\omega\varepsilon_0} \end{aligned} \tag{2.17}$$

where ε_r is the dielectric constant and σ is the conductivity of the RRS medium.

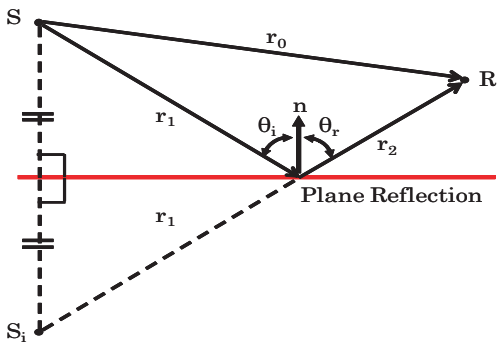

Figure 2.7: Incident and reflected waves.

2.5.2 Source and Image Diffraction Waves

Now we consider the source diffraction shown in Fig.2.8. We assume here that the electromagnetic fields due to the source diffraction can be approximated by the Wiener-Hopf solution to the plane wave diffraction by a perfectly conducting semi-infinite half plane [23]. We omit the field expressions for H-wave for brevity, and the results are summarized as follows [11]:

$$E_z = \begin{cases} E_z^s - D(r,r_0)\Psi(r) & (\text{RegionI}) \\ D(r,r_0)\Psi(r) & (\text{RegionII}) \end{cases} \tag{2.18}$$

where $r = r_1 + r_2$ and the diffraction coefficient is given by

$$\begin{aligned} D(r,r_0) &= e^{jX^2}F(X) \\ X &= \sqrt{\kappa(r-r_0)}\,. \end{aligned} \tag{2.19}$$

The complex type of Fresnel function is defined by [23]

$$F(X) = \frac{e^{\frac{\pi}{4}j}}{\sqrt{\pi}}\int_X^\infty e^{-ju^2}du \quad (X>0)\,. \tag{2.20}$$

This function has the following analytical properties:

$$\begin{aligned} F(X) &= 1 - F(-X) \quad (X<0) \\ F(X) &\simeq \frac{e^{-\frac{\pi}{4}j}}{2\sqrt{\pi}X}e^{-jX^2} \quad (X \gg 1)\,. \end{aligned} \tag{2.21}$$

Finally we consider the image diffraction shown in Fig. 2.9 where the space is divided into three parts, Region I, II and III. In this case, we can summarize the image diffraction coefficients as follows:

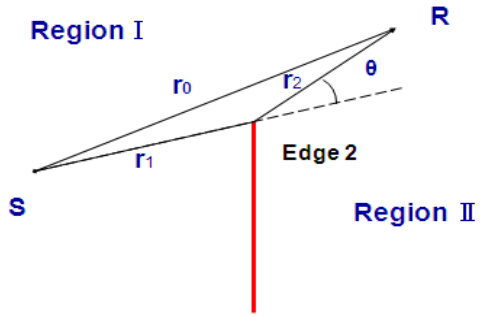

Figure 2.8: Source diffraction by an edge.

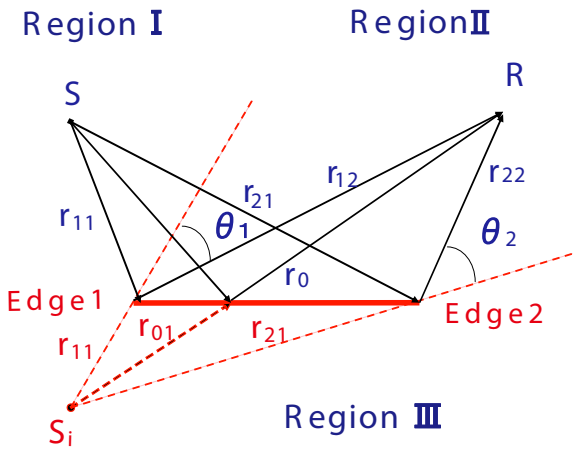

Figure 2.9: Image diffraction by a plate.

$$E_z = \begin{cases} R^h(\theta)[D(r_1,r_0)\Psi(r_1) - D(r_2,r_0)\Psi(r_2)] & (RgionI) \\ R^h(\theta)[\Psi(r_0) - D(r_1,r_0)\Psi(r_1) - D(r_2,r_0)\Psi(r_2)] & (RegionII) \\ R^h(\theta)[D(r_2,r_0)\Psi(r_2) - D(r_1,r_0)\Psi(r_1)] & (RegionIII). \end{cases} \tag{2.22}$$

where $r_0 = r_{01} + r_{02}$, $r_1 = r_{11} + r_{12}$ and $r_2 = r_{21} + r_{22}$. It should be noted that the conventional reflection ray is included in the image diffraction ray in region II resulting in simplification of the proposed DRTM. As mentioned in previous section, the image diffraction is employed when the source, receiver and the representative point at the discretized plate are all in LOS. In other cases, the source diffraction is used for the field computations.

2.5.3 Total Electric Fields

We have discussed the principle of DRTM algorithm to evaluate electric field approximately. The electric field E at the receiver is formally expressed in the following dyadic and vector form:

$$E = \sum_{n=1}^{N} \left[\prod_{m=1}^{m=M_n^i} (D_{nm}^i) \cdot \prod_{k=1}^{k=M_n^s} (D_{nk}^s) \cdot E_0 \right] \frac{e^{-\kappa r_n}}{r_n} \tag{2.23}$$

where E_0 is the electric field of the incident wave at the first source or image diffraction point given by Eq.(2.14). N is the total number of rays considered, M_n^s is the number of times of source diffractions, and M_n^i is the number of times of image diffractions of the n-th ray. The distance of the n-th ray from source to receiver is given by

$$r_n = \sum_{k=0}^{k=M_n^i+M_n^s} r_{nk} \quad (n = 1,2,\ldots,N) \tag{2.24}$$

where r_{nk} is the k-th distance from a source or an image diffraction point to another.

In the numerical simulations, we select dielectric constants. As mentioned above, the reflection coefficients include the dielectric constants, but the diffraction coefficients are for perfect conductors and it dose not include those dielectric parameters. We have already analyzed the numerical accuracy by comparing with the experimental results, and we have demonstrated that the numerical solutions have a good accuracy [25].

2.6 Conclusion

We have reviewed the theory of DRTM in this chapter. Since we need various kinds of RRS when we analyze different kind of propagation environments for DRTM analysis, we have firstly described convolution method that numerically generates many kind of RRS characterised by two parameters, correlation length (cl) and height deviation (dv). We have secondary described the principle of discretization of rough surface and ray tracing, and finally we have described the theory of field computation. The general essence of DRTM is to discretize not only RRS but also ray tracing. The former helps saving computer memory and the latter simplify the ray searching algorithm resulting in saving computation time.

Chapter 3

Evaluation of DRTM

3.1 Introduction

We evaluate DRTM and apply to the EM wave scattering by a cylindrical conductor or by a conducting half-plane, and we check the accuracy of DRTM by comparing its results with rigorous analytical solutions. In case of a cylinder, its boundary is approximated in terms of piecewise-linear plates, and source and image rays are searched based on the approximated profile. The total scattered fields are given by superposing each scattered field related to each plate which is computed by use of the source and image diffraction coefficients obtained by the Fresnel function. In case of a half-plane, the total scattered fields are computed rigorously by using the Fresnel function.

In the former evaluation case, numerical results are compared with the rigorous solutions given by use of the Bessel and Hankel functions. In the latter evaluation case, numerical computations are performed to check the effect of diffraction points on the field distributions in shadow region. It is demonstrated that DRTM provides us a good convergence. We add explanations for two types of rigorous solutions in the end of this chapter; one is rigorous solution to the plane-wave diffraction by a conducting cylinder, and the other is rigorous solution to the plane-wave diffraction by a conducting half-plane .

3.2 Geometry of the Problem

Figure 3.1 shows the geometry of the problem. Although the source is located at left hand side in this Figure, of course its location may be arbitrary. Originally the cross section of

the cylinder is circle (red), but it is approximated in terms of piecewise-linear plates (blue) as shown in the Figure where the number of plates has been chosen as $N = 8$. Moreover, the radius of the cylinder is denoted by a, and the observation points are located on the circle (green) of radius r.

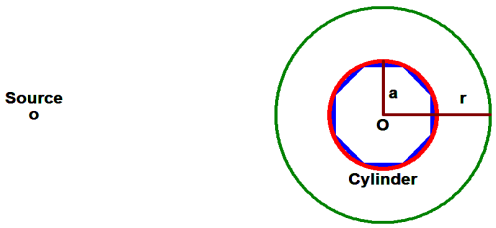

Figure 3.1: Geometry of the problem.

In this chapter, we deal with scattering of the plane-wave by a perfectly conducting cylinder and a conducting half-plane. It is assumed that the structure is uniform in z-direction or two-dimensional (2D). We consider that the scattered field is defined by the total field (t) minus the source or incident field (s), that is, $(E,H) = (E^t,H^t) - (E^s,H^s)$.

3.3 Scattered Rays and Fields from the Cylinder

Figure 3.2 shows some source diffraction rays from an edge at the upper side of the cylinder. The cylinder of radius $5[m]$ with its centre at the origin $(x,y) = (0,0)$ is divided into 36 plates, and the source is located at $(x,y) = (-1000,0)[m]$. Receiving points are located at the circle of radius $10[m]$, the operating frequency is selected as $f = 300[MH_z]$.

In addition to the source diffraction from the upper side, other rays caused by the source diffraction from a lower edge are included in Figure 3.3.

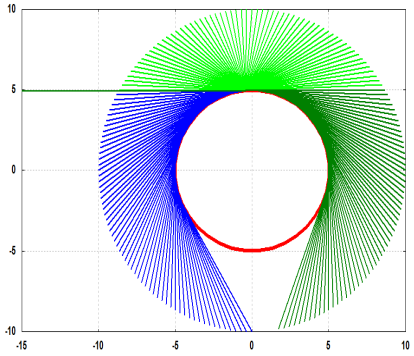

Figure 3.2: Source diffraction rays from an edge at the upper side.

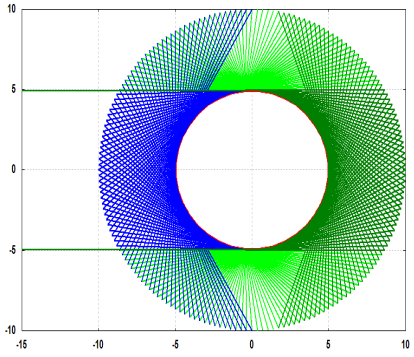

Figure 3.3: Source diffraction rays from both edges at the upper and lower sides.

Figure 3.4 shows electric field distribution for E-wave computed by using only the source diffraction rays shown in Figure 3.3. In this case the fields are computed by

$$\begin{aligned} E_z^{sd} &= \sum_{n=1}^{2} E_z^{sd}(n) \\ H_z^{sd} &= \sum_{n=1}^{2} H_z^{sd}(n) \end{aligned} \tag{3.1}$$

where $n = 1$ and $n = 2$ correspond to source diffractions from the upper and lower edges, respectively. It should be noted that the minus source or incident field has been assumed in the shadow region. We explain rigorous solutions in section 3.6.

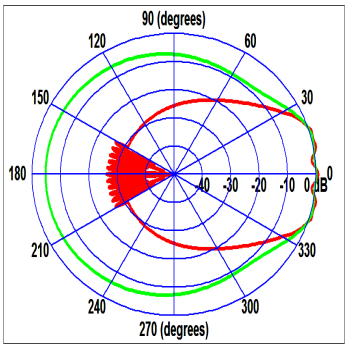

Figure 3.4: Source diffraction field (red) in comparison with the rigorous solution (green).

Figure 3.5 shows some image diffraction rays from one plate in the illuminated region; in this example, the image diffraction occurs at the 18-th plate corresponding to $k = 18$ in Eq.(3.2). The source point and the receiving points are chosen as the same as in Figure 3.2. Figure 3.6 shows image diffraction rays obtained by considering all the illuminated plates; in this example, the image diffractions occur at plates corresponding to $k = 10$ through $k = 26$.

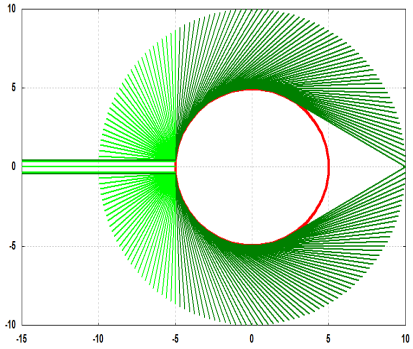

Figure 3.5: Image diffraction rays from one illuminated plate.

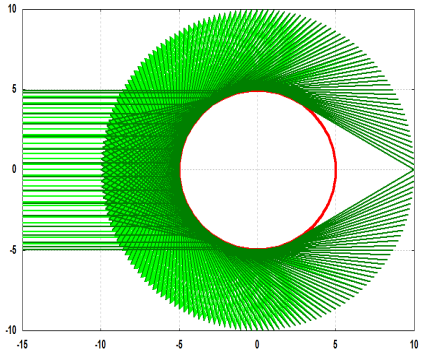

Figure 3.6: Image diffraction rays from all the illuminated plates.

Figure 3.7 shows electric field distribution for E-wave computed by summing up the results obtained by Eqs.(2.22) using only the image diffraction rays shown in Figure 3.6. These field computations are carried out by

$$\begin{aligned} E_z^{id} &= \sum_{k=1}^{K} E_z^{id}(k) \\ H_z^{id} &= \sum_{k=1}^{K} H_z^{id}(k) \end{aligned} \tag{3.2}$$

where K is the total number of illuminated plates.

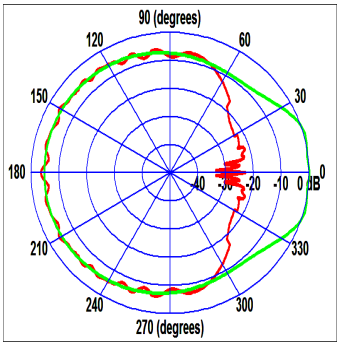

Figure 3.7: Image diffraction field (red) in comparison with rigorous solution (green).

Finally we can obtain the total scattered fields by adding the source diffraction fields and the image diffraction fields as follows:

$$\begin{aligned} E_z &= E_z^{sd} + E_z^{id} \\ H_z &= H_z^{sd} + H_z^{id} \ . \end{aligned} \tag{3.3}$$

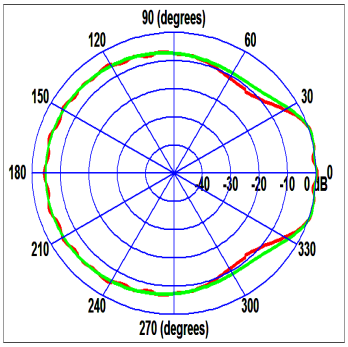

Figure 3.8: Scattered E-wave obtained by DRTM with 36 plates (red) in comparison with rigorous solution (green).

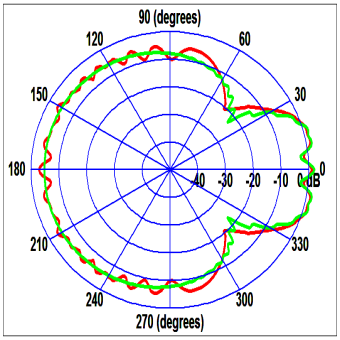

Figure 3.9: Scattered H-wave obtained by DRTM with 36 plates (red) in comparison with the rigorous solution (green).

Figure 3.8 and Figure 3.9 show scattered fields for E-wave and H-wave, respectively. It is shown that a better accuracy is achieved in case of E-wave than in case of H-wave.

3.4 Field Convergence and Number of Plates

Figure 3.10 shows scattered electric fields when the radius of the cylinder has been chosen as $a = 10[m]$ and the observation points have been selected on the circle with radius $r = 20[m]$. In this Figure, we have shown two types of cylinder discretizations for DRTM; one is with 36 plates and the othr is with 72 plates, respectiely. It is shown that the DRTM solution with 72 plates exhibits a little more accurate numerical result than that with 36 plates.

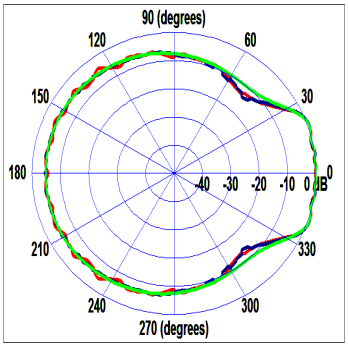

Figure 3.10: Scattered E-wave obtained by DRTM with 36 (red) and 72 (blue) plates in comparison with rigorous solution (green).

Figure 3.11 shows scattered magnetic fields with the same parameters as the former example. In this Figure, we have shown two types of cylinder discretizations for DRTM; one is with 36 plates and the othr is with 72 plates, respectiely. It is shown that the DRTM solution with 72 plates exhibits a little more accurate numerical result than the other case with 36 plates. Moreover, it is demonstrated that results based on DRTM in case of H-wave show a poorer accuracy than those in case of E-wave.

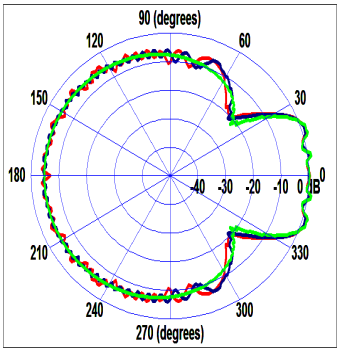

Figure 3.11: Scattered H-wave obtained by DRTM with 36 (red) and 72 (blue) plates in comparison with rigorous solution (green).

Figure 3.12 shows root mean square errors of DRTM solutions in comparison with the rigorous solutions for the EM wave scattering by a conducting cylinder [27]. The parameters used are such that the operating frequency is $f = 300$ [MHz] with corresponding wavelength $\lambda = 1$ [m], the radius of conducting cylinder is $a = 10$ [m] with corresponding circumference $\ell = 62.8$ [m] and the observation points are at r=20 [m] from the centre of the conducting cylinder. Moreover, the red line in this figure indicates E-polarized incidence and the blue line denotes H-polarized incidence.

It is demonstrated that the errors in case of H-wave are almost double of those in case of E-wave, and the error suddenly increases when the number of plates decreases into less than 30 plates. This means that we should keep the plate length Δx shorter than twice of the wave length. According to these numerical examples, the minimum error rate is about 5.9 % when the plate number is 140-220, when the plate length Δx is chosen as same as from 29 % to 45 % of the wave length, good accuracies are obtained.

And better accuracies are not achieved even if the boundary is divided into smaller pieces, in other words, the error gradually increases when the plate number becomes

more than 220 plates. It is shown from the numerical examples that the minimum error has been achieved for $\Delta x \simeq \lambda$. Thus, it is concluded that $\lambda \geq \Delta x$ is required for field computations by use of DRTM.

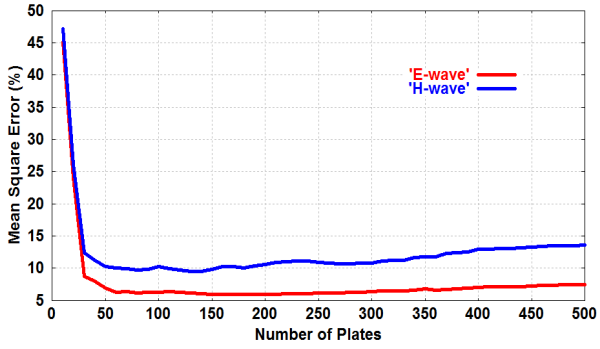

Figure 3.12: Mean square errors of DRTM solutions compared with rigorous solutions.

3.5 Rigorous solutions

In this section, we explain two types of rigorous solutions which are noted through section 3.2 to 3.4.

3.5.1 Rigorous solution to the plane-wave diffraction by a conducting cylinder

In this section we show the rigorous solutions in terms of Bessel and Hankel functions for the plane wave scattering by a perfectly conducting cylindrical rod [24]. Assuming that a plane wave $e^{-j\kappa(x\cos\theta_i + y\sin\theta_i)}$ with incident angle θ_i is incident upon a conducting

cylinder of radius a, we have the rigorous solution for the scattered E-wave as follows:

$$E_z = -\sum_{n=-\infty}^{\infty} \frac{J_n(\kappa a)}{H_n^{(2)}(\kappa a)} H_n^{(2)}(\kappa r) \times e^{jn(\Theta-\theta_i-\pi/2)} \tag{3.4}$$

where $J_n(x)$ is the Bessel function of the $n-th$ order, and $H_n^{(2)}(x)$ is the second kind of Hankel function of the $n-th$ order. It should be noted that we have employed the polar coordinates (r,Θ) having the relations with the Cartesian coordinates (x,y) such as $x = r\cos\Theta$ and $y = r\sin\Theta$.

On the other hand we have the rigorous solution for the scattered H-wave as follows:

$$H_z = -\sum_{n=-\infty}^{\infty} \frac{J_n'(\kappa a)}{H_n^{(2)'}(\kappa a)} H_n^{(2)}(\kappa r) \times e^{jn(\Theta-\theta_i-\pi/2)} \tag{3.5}$$

where the prime of the Bessel or the Hankel function denotes the derivative of the function with respect to their argument.

3.5.2 Rigorous solution to the plane-wave diffraction by a conducting half-plane

It is well-known that the plane wave diffraction by a conducting half plane can be solved rigorously by use of the Winer-Hopf technique [23]. The results are compactly expressed in terms of the complex type of Fresnel function defined in Eq.(2.21). Since the Winer-Hopf solutions to the plane wave diffraction by a conducting half-plane are considered to be the basis of the DRTM, we summarize the final results in the following.

The geometry of the problem is shown in Figure 5.1 where the half-plane is uniform in z-direction (two-dimensional) and we select the edge point as $(A = B = 0)$ so that the edge coincides with the origin. Then we have the field expression for E-wave with the reflection coefficient $R^e = -1$ as follows:

$$E_z^t(x,y) = \begin{cases} D_s(X_s)e^{-j\kappa r} + R^e D_i(X_i)e^{-j\kappa r} & (\theta_i < \Theta < \pi) \\ e^{-j\kappa r\cos(\Theta-\theta_i)} - D_s(X_s)e^{-j\kappa r} + R^e D_i(X_i)e^{-j\kappa r} & (-\theta_i < \Theta < \theta_i) \\ e^{-j\kappa r\cos(\Theta-\theta_i)} - D_s(X_s)e^{-j\kappa r} + R^e e^{-j\kappa r\cos(\Theta+\theta_i)} & \\ -R^e D_i(X_i)e^{-j\kappa r} & (-\pi < \Theta < \theta_i) \end{cases} \tag{3.6}$$

Moreover, we have the field expression for H-wave with the reflection coefficient $R^h = 1$ as follows:

$$H_z^t(x,y) = \begin{cases} D_s(X_s)e^{-j\kappa r} + R^h D_i(X_i)e^{-j\kappa r} & (\theta_i < \Theta < \pi) \\ e^{-j\kappa r\cos(\Theta_i^\theta} - D_s(X_s)e^{-j\kappa r} + R^h D_i(X_i)e^{-j\kappa r} & (-\theta_i < \Theta < \theta_i) \\ e^{-j\kappa r\cos(\Theta-\theta_i)} - D_s(X_s)e^{-j\kappa r} + R^h e^{-j\kappa r\cos(\Theta+\theta_i)} & \\ -R^h D_i(X_i)e^{-j\kappa r} & (-\pi < \Theta < \theta_i) \end{cases} \tag{3.7}$$

where the diffraction functions are given by

$$\begin{aligned} D_s(X_s) &= e^{jX_s^2}F(X_s) \\ D_i(X_i) &= e^{jX_i^2}F(X_i) \end{aligned} \tag{3.8}$$

and

$$\begin{aligned} X_s &= \sqrt{\kappa r[1-\cos(\Theta-\theta_i)]} \\ X_i &= \sqrt{\kappa r[1-\cos(\Theta+\theta_i)]}\,. \end{aligned} \tag{3.9}$$

3.6 Conclusion

We have evaluated DRTM, applying the source and image diffraction coefficients to the EM wave scattering by a cylindrical conductor to check the accuracy of DRTM since we have rigorous analytical solutions to be compared with. We also evaluate DRTM with the plane wave diffraction by a conducting half-plane since the scattered field for this problem can be computed rigorously by using the Fresnel function.

Numerical examples have been given for the source and image diffraction rays as well as the field distributions. Accuracy of DRTM has been discussed in comparison with the rigorous solutions focussing on the number of plates discretizing the cylinder. It has been demonstrated that DRTM has a good accuracy and there exists an appropriate optimal number for the cylinder discretization.

Chapter 4

Application to Long Distance Propagation

4.1 Introduction

In this chapter, we apply DRTM to the long distance propagation analysis of terrestrial digital TV waves and we apply GIS to obtain surface profile data. In Fukuoka area, the terrestrial digital TV has been broadcasting from Fukuoka tower which is the highest buildings in the local area and located at the central part of Fukuoka city. However, the city is surrounded by mountains except for the northern part of sea side, therefore there exist some blind zones where the base stations cannot cover. As a result, relay stations should be constructed to overcome the blind zone problems. In this chapter, we estimate electric field distributions from three sources; main station at Fukuoka tower and two relay stations at Mt. Kaya and Fukae area.

We have two steps of field estimation procedure in this chapter. First, we apply the GIS system to obtain surface profile data. Second, we apply the DRTM to compute electric field distributions along the straight line between the two points. By numerical results of the DRTM, we have recognized the performance of existing two relay stations for those areas. The relay station at the top of Mt. Kaya covers Maebaru area which is in the west direction from Fukuoka city. The relay station in Fukae can cover only a small area due to so little input power. We have confirmed that the DRTM has a good performance to estimate EM fields for long distance propagation.

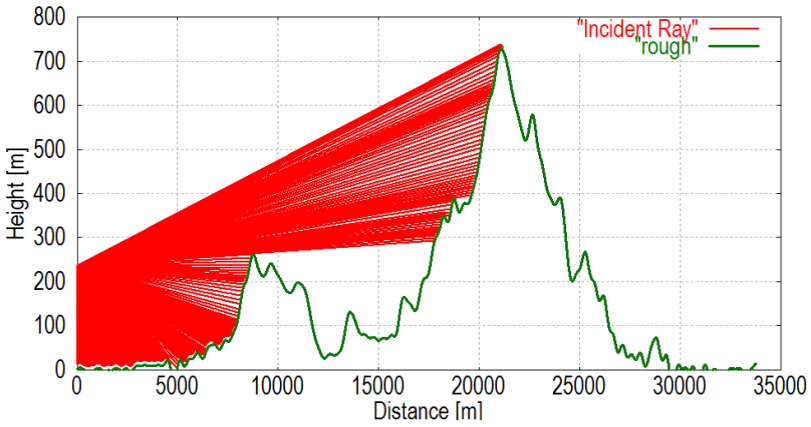

Figure 4.1: Incident rays in the region of LOS.

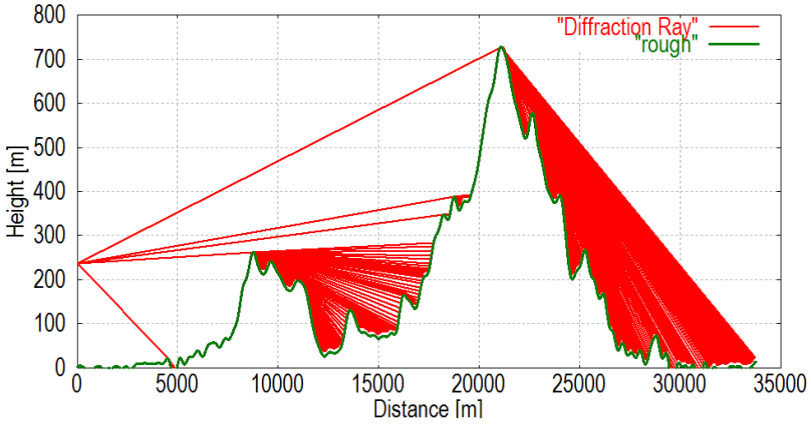

Figure 4.2: Diffraction rays in the region of NLOS.

4.2 Incident Rays and Diffraction Rays

Figure 4.1 shows an example of incident rays in the region of LOS corresponding to the 0th order rays. Figure 4.2 shows an example of diffraction rays in the region of NLOS corresponding to the 1st order rays. Reflected rays of the 1st order and reflected and/or diffracted rays of the second order are omitted in these figures. As we can see here, the incident rays are dominated in open area or LOS region as shown in Figure 4.1, and the diffraction rays are dominated in shadow area or NLOS region as shown in Figure 4.2.

4.3 Import of Terrain Profile Data

We introduce GIS to import the terrain profile data. The GIS is a integrated system for analyzing and displaying all forms of geographically referenced information that allows us to view, understand and visualize data in many ways that reveal relationships in the form of maps and the information. The GIS helps our methods of collecting data and carrying out the propagation analysis.

The proposed procedure for importing terrain data is composed of two steps. The first step is to import a sampling data for the terrain profile, and second one is to convert the data to continuous numerical terrain data.

4.3.1 Import of sampling data

We can obtain the sampling data for the terrain profile between two designated points by applying the GIS. In Figure 4.3 a screen shot of the system is shown, we can get the sampling data for the terrain profile between the two designated points. In this Figure, one point is at Fukuoka tower and the other point is at Maebaru beyond Mt. Kaya. After selecting two points, we have the sampling data for the required terrain profile as shown in Figure 4.4. The sampling data cannot be straightforwardly applied to DRTM, so that we have to convert the data to a continuous numerical data. Thus we can import the numerical data $\{x_m, y_m\}$ $(m = 0, 1, 2, \cdots, M)$ as a text file.

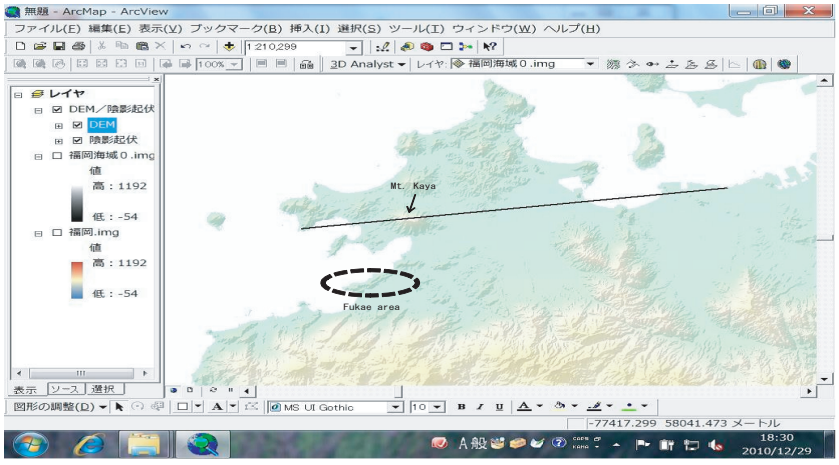

Figure 4.3: A screen shot of *GIS*.

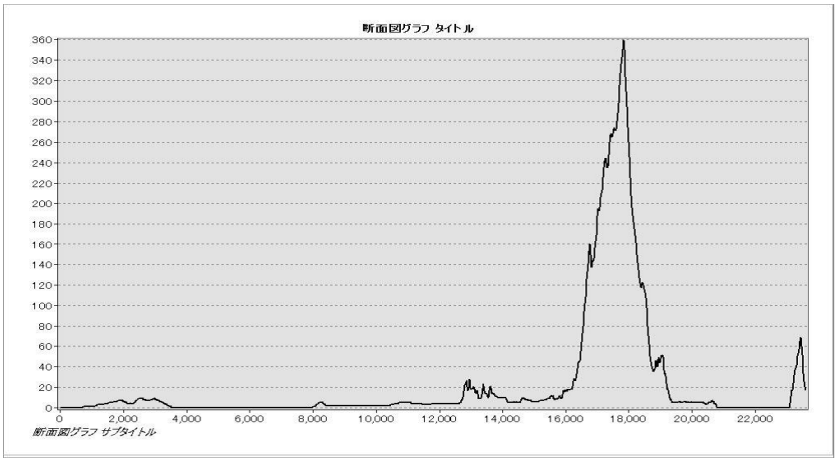

Figure 4.4: Sampling data for a required terrain profile.

4.3.2 Regeneration of a continuous terrain profile

We assume that the interval of the numerical data in x-direction to be D_x, that is, $x_m = mD_x \quad (m = 0,1,2,\ldots,M)$. Then we can introduce an approximate height function for the terrain profile data regeneration as follows:

$$f(x) = \sum_{m=0}^{m=M} y_m \frac{\sin[\pi(x/D_x - m)]}{[\pi(x/D_x - m)]}. \tag{4.1}$$

Eq.4.1 provides an approximate but continuous terrain profile, and we can easily apply the height data obtained by this equation to a DRTM simulation. Figure 4.5 shows an approximated terrain profile regenerated by Eq.4.1. It is demonstrated that the regenerated numerical data illustrated in Figure 4.5 is in good agreement with the sampling data illustrated in Figure 4.4.

4.4 DRTM simulations for field distributions

Figure 4.6 shows the geometry of the problem. In the present DRTM simulations, we have assumed that there exists a sea surface in the region from $x = 3km$ to $7km$ and other regions are occupied by a dry ground surface. The antenna of main station is located on Fukuoka tower at $x = 0m$ and $y = 234m$, and the relay station transmitter is located at $5m$ above the top of Mt. Kaya ($365m$). In the numerical simulations, we have assumed that the observational points are $5m$ above the sea or ground surface. Frequency is selected as $f = 527.0MHz$ which is the operating frequency of NHK terrain digital broadcasting

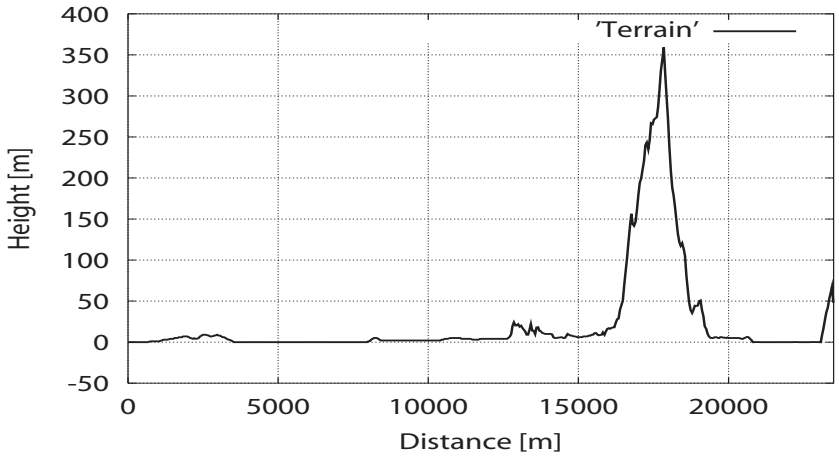

Figure 4.5: Regenerated curve for the terrain profile.

service. Input powers are $3KW$ and $30W$ at the Fukuoka tower and Mt. Kaya, respectively.

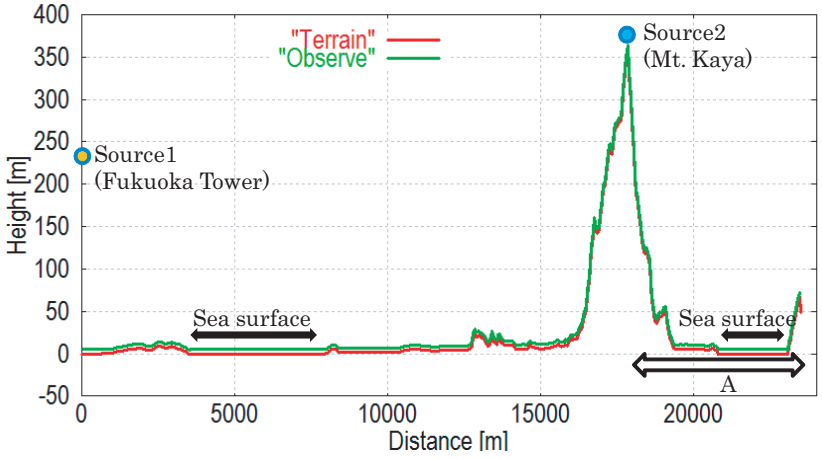

Figure 4.6: Geometry of the problem.

Figs.4.7 and 4.8 show the electric field intensities radiated from the main station at Fukuoka tower and the relay station at Mt. Kaya, respectively. It is shown in Figure 4.7 that the field intensity radiated from the main station is decaying apart from the station, but it keeps relatively high level due to the high input power ($3KW$). Because of the shadowing effect of a mountain near at $x = 19Km$, however, there exists a blind zone A where electric field intensities are below $-60dB$. On the other hand, Figure 4.8 shows

that the field intensities radiated from the relay station are much higher than $-60dB$ at the region A, and thus the relay station covers the blind zone effectively.

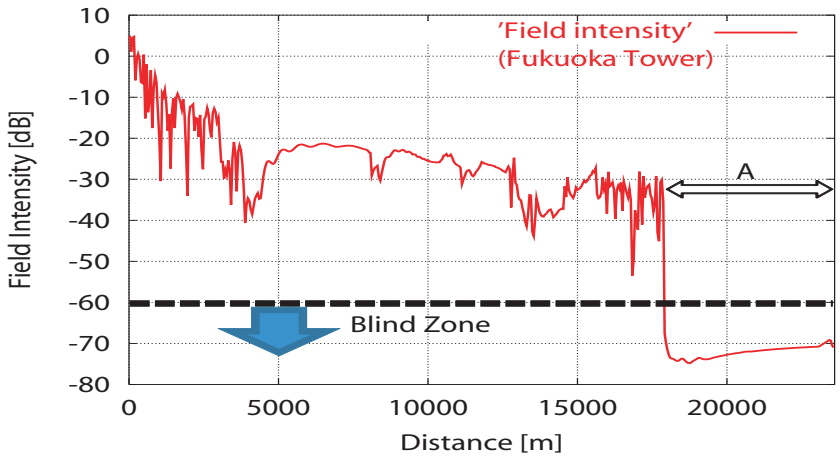

Figure 4.7: Intensity of radio wave emitted from the main station at the Fukuoka tower.

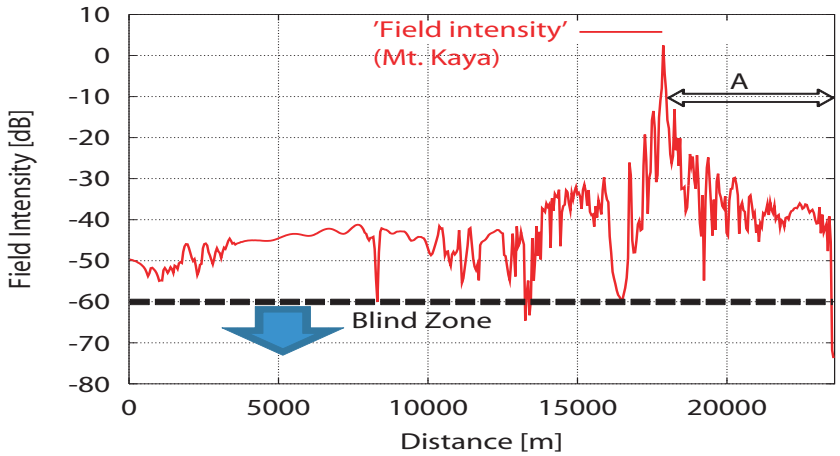

Figure 4.8: Intensity of radio wave emitted from the relay station at Mt. Kaya.

In Figure 4.9, we have compared the field distribution radiated from the main station with that from the relay station. In Figure 4.10, we have shown only the maximum part of the two field distributions radiated from the main and relay stations. It is well demonstrated that the field intensity level in Figure 4.10 is much higher than $-60dB$ almost everywhere in the range $0 < x < 25km$.

Figure 4.11 shows the incident rays emitted from the main station. Figure 4.12 shows field distributions of the radio wave radiated from the main station. It is shown that

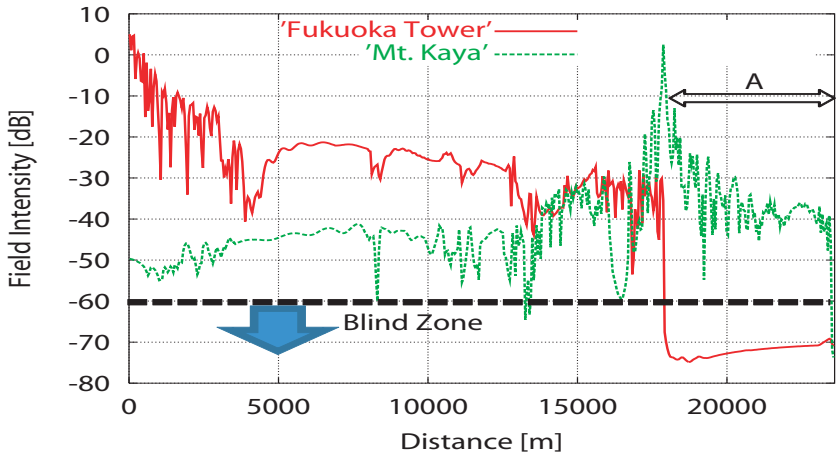

Figure 4.9: Intensities of radio waves emitted from the main and relay stations.

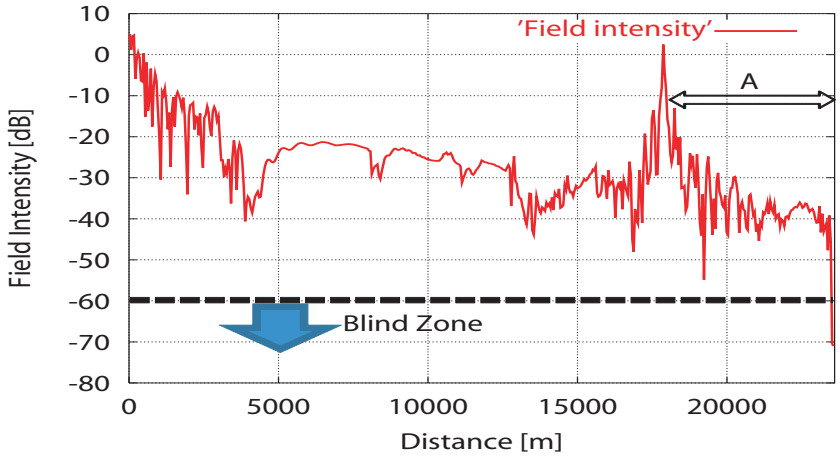

Figure 4.10: Maximum part of the two radio waves emitted from the main and relay stations.

incident rays reach the top of Mt. Kaya where the relay station is located, and some degree of field decays are observed in the shadow regions.

Figure 4.13 shows incident rays emitted from the relay station at Mt. Kaya. Figure 4.14 shows field distributions of the radio wave radiated from the relay station. It is shown that some degree of field decays are observed in the shadow region. Reflected waves from the sea surface are also observed between $3km < x < 7Km$. Comparison of Figure 4.12 with Figure 4.14 reveals clearly that the blind zone of the main station is cancelled by the radiation from the relay station.

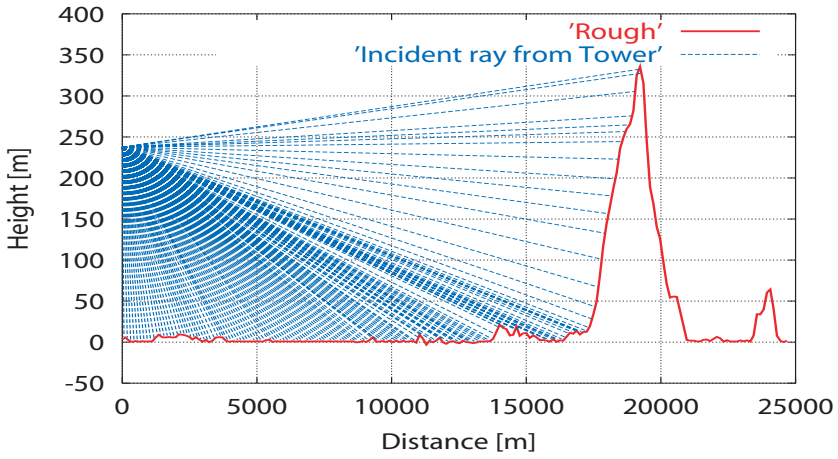

Figure 4.11: Incidence rays in LOS from the main station at the Fukuoka tower.

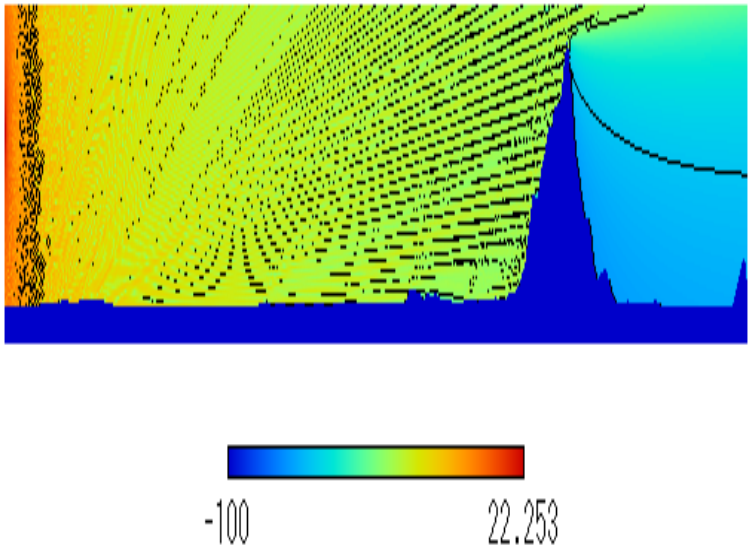

Figure 4.12: 2D field distributions from the main station at the Fukuoka tower.

Next, we consider other area in western part of Fukuoka. Fukae area is located at southern part of Mt. Kaya. Figures 4.15 and 4.16 show geometry of the problem and field intensities radiated from the Fukuoka tower. In these Figures, Fukae area is located at near x=20km. Because of the shadowing effect of mountain near x=10km, there exist a blind zone in Fukae area. To overcome this problem, the relay station at Mt. Kaya plays an important role.

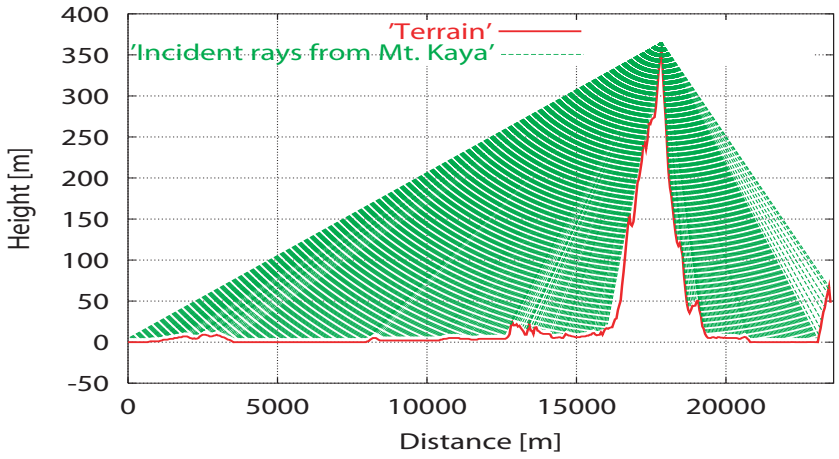

Figure 4.13: Incident rays in LOS from the relay station at Mt. Kaya.

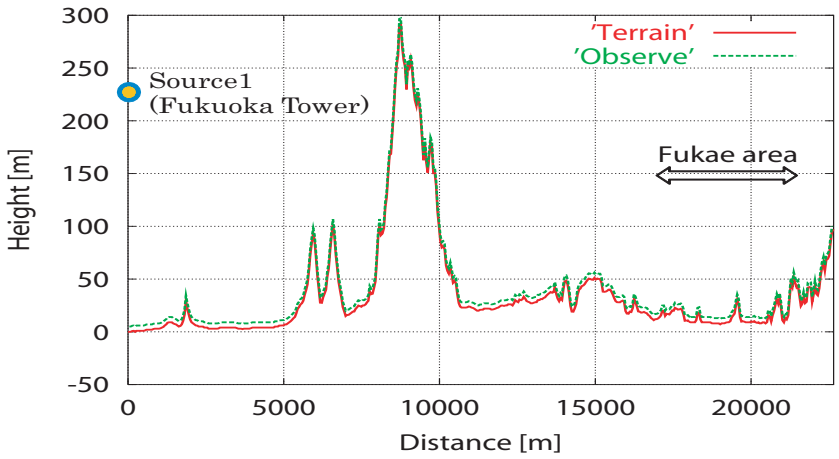

Figure 4.15: Geometry of the problem (from Fukuoka tower to Fukae area).

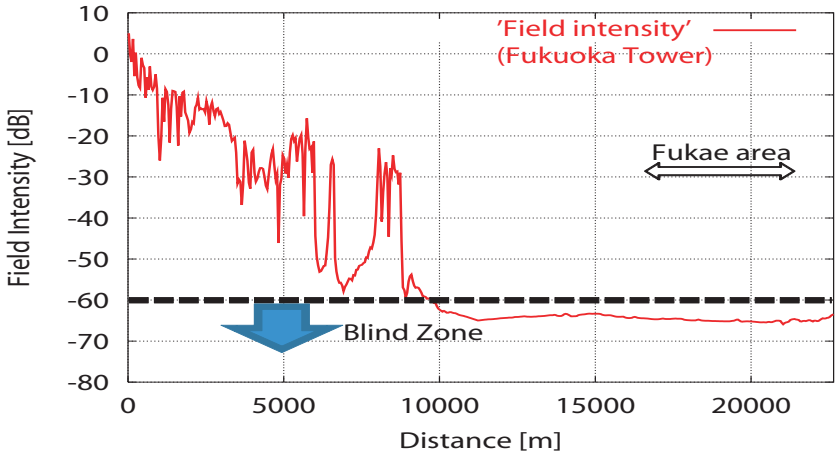

Figure 4.16: Intensity of radio wave emitted from the Tower.

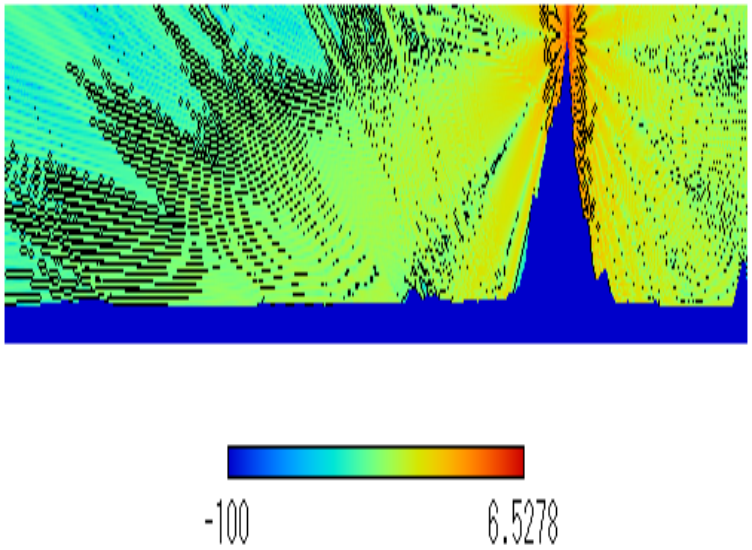

Figure 4.14: 2D field distributions radiated from the relay station at Mt. Kaya.

Figures 4.17 and 4.18 show geometry of the problem and field intensities radiated from the relay station at Mt. Kaya. It is shown that even though the field intensities from Mt. Kaya keeps high level, there exists a new blind zone beyond the hills. Therefore, another relay station is required to overcome the new blind zone.

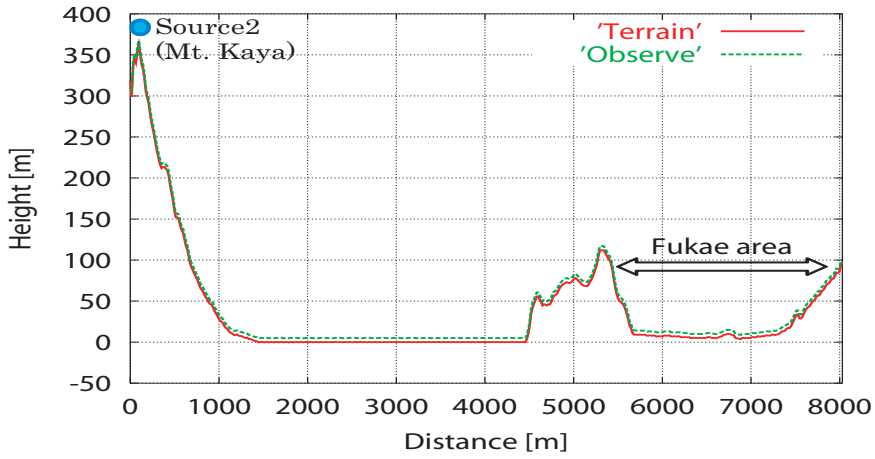

Figure 4.17: Geometry of the problem (from Mt. Kaya to Fukae area).

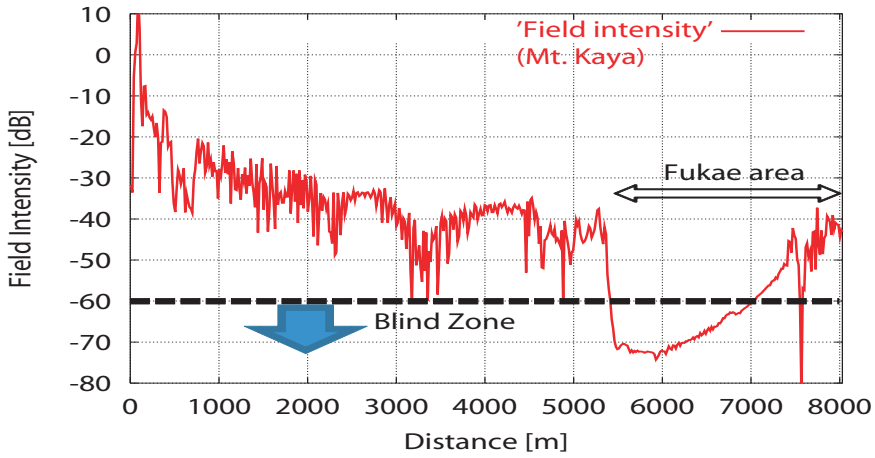

Figure 4.18: Intensity of radio wave emitted from the relay station at Mt. Kaya.

Figures 4.19 and 4.20 show geometry of the problem and field intensities radiated from a small relay station at Fukae. It is shown that the new blind zone is cancelled by the small relay station with the input power of which is only $50[mW]$. As a result, it is found that the blind zone from the relay station can be cancelled by another relay station installed with so small input power.

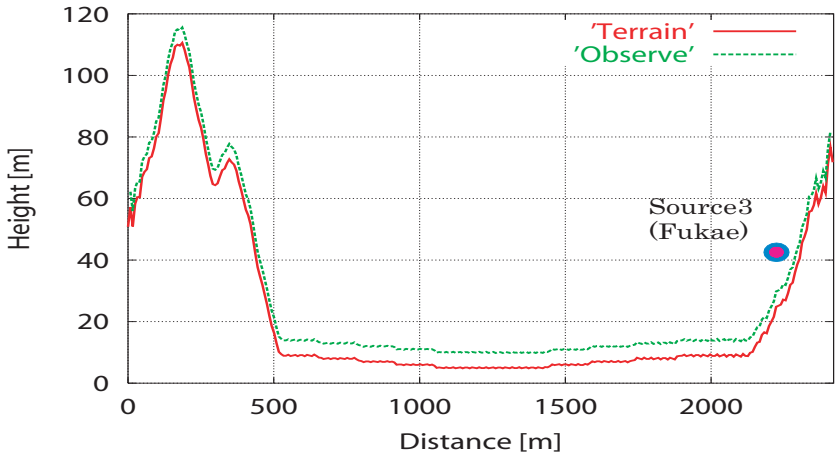

Figure 4.19: Geometry of the problem (Fukae area).

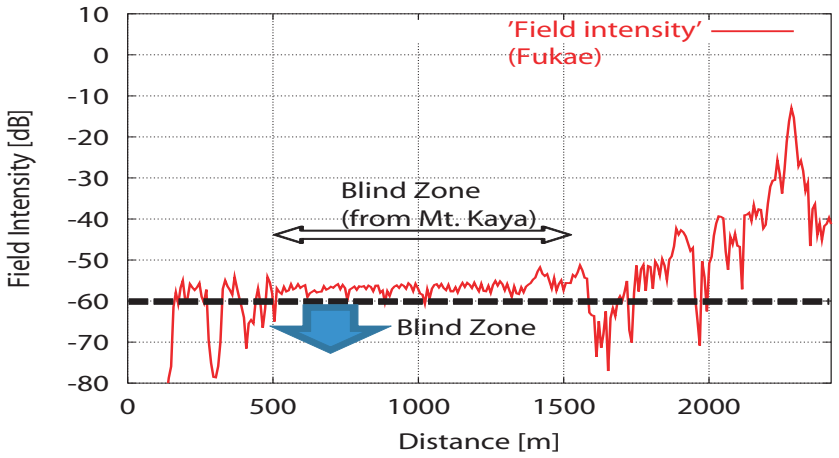

Figure 4.20: Intensity of radio wave emitted from a small relay station at Fukae area.

Results of numerical simulations shown so far are summarized as follows. Even though the main station's input power level is high, the electric field intensities in the NLOS region are generally small, where there may exist some blind zones. However, these blind zones can be clearly and effectively cancelled by the relay station installed at

a high position which is in LOS of the main station. If the relay station can not cover the blind zone, another one with small input power is required to install.

4.5 Conclusion

In this chapter, we have applied DRTM to analyze long distance propagation, importing the terrain profile data by using GIS, and we have carried out numerical simulations for electric field distributions of the radio wave from the main station at the Fukuoka tower as well as the radio waves from the relay stations at Mt. Kaya and at Fukae area.

It has been demonstrated that the blind zones of the main station are clearly and effectively cancelled by relay stations located at appropriate positions. It has been also shown that another relay station with small input power is required if the relay stations can not cover the blind zones perfectly. Thus it can be concluded that the DRTM is significantly useful to solve a long distance propagation problem and to make a decision where we should allocate some relay stations efficiently.

Chapter 5

Edge Points and Sampling Rate

5.1 Introduction

In this chapter, we investigate the relationship between the diffraction phenomenon at edge points near the summit and discretization rate at there. In the DRTM simulation, fewer sampling rate of the terrain profile decreases the computation time and taking this method surely helps us to save the time for simulating the long distance propagation problems. However, we have to pay careful attention to the diffraction phenomenon at the edge point near the summit, because, the diffraction phenomenon diversely affects field distributions especially in shadowing area following the summit. Considering the phenomenon at the summit, we propose to take an intensive sampling rate at the summit to get accurate simulation and a fewer sampling rate in the plain area to decrease the computation time. We also discuss the importance to coincide the edge points near the summit with the real positions of the terrain surface when we apply the DRTM simulation.

5.2 Diffraction points on the field distributions in shadow region

Figure 5.1 shows a geometry depicting the plane wave diffraction by a conducting half-plane of which edge point (A,B) is variable. The observation points are along a straight line from the origin $(0,0)$ in the direction parallel to the plane wave incidence.

Figure 5.2 shows electric field distributions in case of E-wave with different four edge points as $(A,B) = (0,-1),(1,-1),(2,-1)$ and $(3,-1)[m]$, respectively. The incident an-

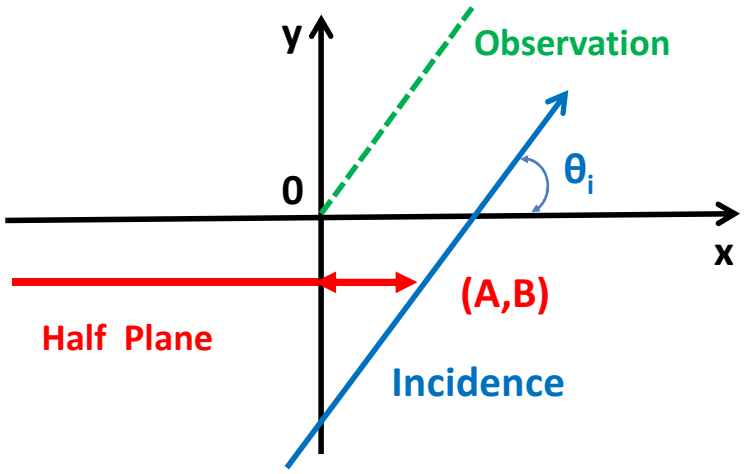

Figure 5.1: Half plane and observation points along incidence in shadow region.

gle is chosen as $\theta_i = 45^\circ$ and the operating frequency is selected as $f = 300[MH_z]$. It is shown that the diffracted fields are strongly influenced by the edge position of the conducting half-plane in the shadow region. Thus it is concluded that the edge points of a disctretized profile should coincide with the diffraction points of the original profile for the diffraction problem to be solved by DRTM.

Figure 5.3 shows magnetic field distributions in case of H-wave. The edge points, the incident angle and the operating frequency are the same as the former examples shown in Figure 5.2. It is shown that the field levels for H-wave are relatively larger than those for E-wave in the shadow region but other characteristics of the field distributions are almost the same as those for E-wave.

5.3 Diffraction at the summit

Figure 5.4 shows two discretized cases of a terrain profile for digital TV broadcasting from Fukuoka to the south. We assume that the source antenna is at the top of Fukuoka tower at 234 [m] high above the ground. Observation points are located at 10 [m] high

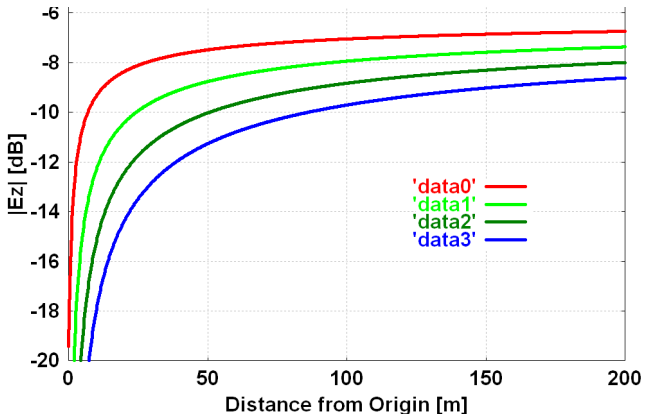

Figure 5.2: Electric fields in the shadow region in case of different diffraction points.

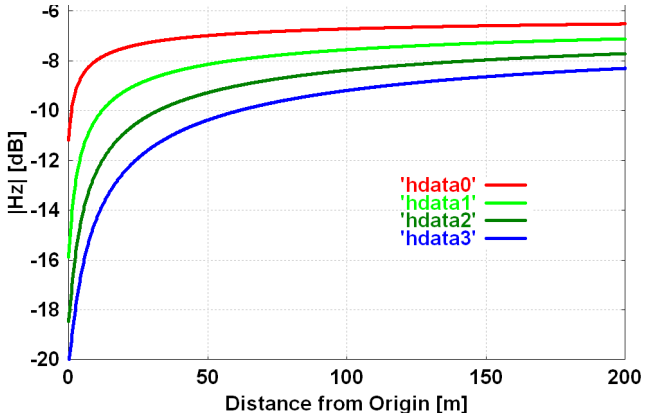

Figure 5.3: Magnetic fields in the shadow region in case of different diffraction points.

above the ground. Red line corresponds to the case where the total distance 30 [km] is divided by 100 points, and thus plate length is 300 [m]. And green line shows the case of 1,000 points with plate length 30 [m].

It is well known that the higher frequency we use, the more propagation loss we have, especially in the shadow region where the diffracted ray dominates the field intensity [26]. Figure 5.5 shows the propagation loss of each frequency from 30MHz to 3GHz. To make this study clear, we neglect the reflection ray in this investigation, only incident ray and diffraction ray are observed.

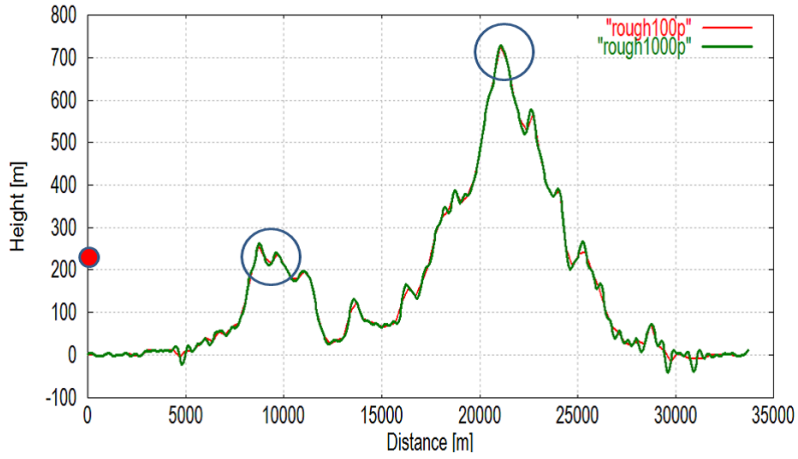

Figure 5.4: Discretization of rough surface.

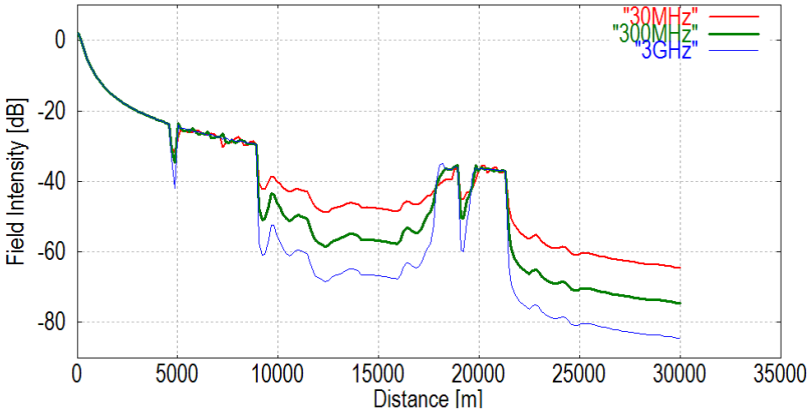

Figure 5.5: Field intensity of each 3 frequencies.

Figure 5.6 is a zoom-in version of the first mountain summit in Figure 5.4, the location of the peak is around 8,800 [m] from the source point. The figure shows two different sampling rate near the mountain summit. The green line has 10 times of the sampling rate of those of the red line, and the diffraction point, the edge point of the red line, is apparently different from the real peak point of the original terrain profile because of insufficient sampling rate. Consequently the difference of edge positions could cause ray errors of DRTM, resulting in field error in shadowing area following the summit.

Figure 5.7 shows electric field distributions computed by DRTM. Frequency is selected as $f = 300[MH_z]$ and the input power of the source antenna is chosen as $P_i = 3[KW]$. Red, green, blue and pink lines correspond to the profile discretization with 200, 500, 1,000 and 10,000 plates, respectively. It is found that accurate EM field estimation even with a small discretization number is obtained in the illuminated regions, but under estimation is observed in the shadow region. We observe fairly good convergence on the field distributions when the plate length is chosen as close as the wavelength, when the whole coverage is divided into 10,000 plates, resulting diffraction points have coincided with original peak points. The numerical error becomes large by decreasing the number od sampling points.

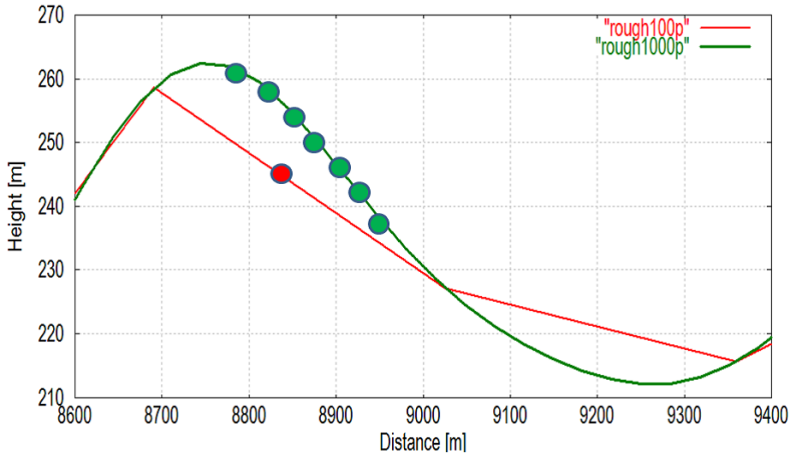

Figure 5.6: The number of sampling points at the summit.

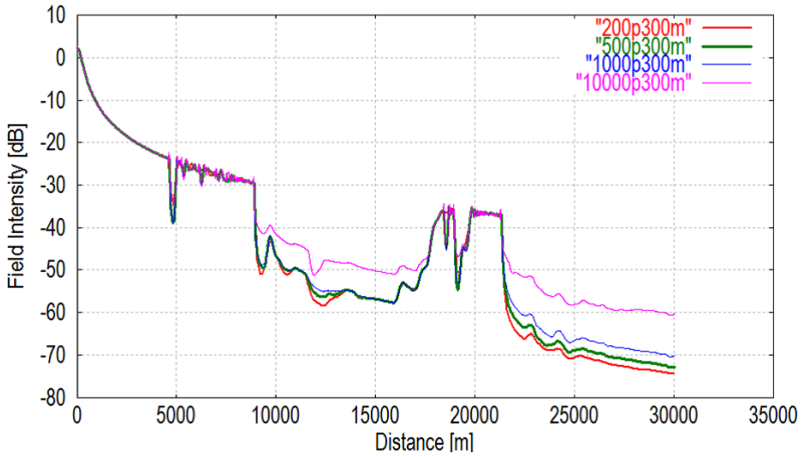

Figure 5.7: Field intensity of 300MHz with different number of sampling rate.

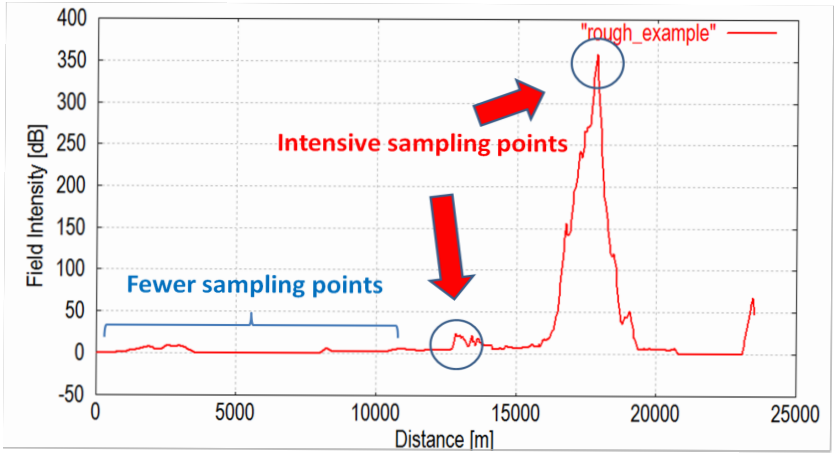

Figure 5.8: How to adjust sampling rate in relation to the geometry information.

5.4 Conclusion

Discretization causes propagation loss in shadow regions because of a lack of sampling rate especially at mountain summits. To address this issue, the author proposes to set the parameters of the discretization rates arbitrarily depending on locations: for example, more sampling rate at the mountain summits and fewer in the plain areas. By setting such parameters, the author postulates that the accuracy of the simulation results will be better and the computation time will be shorten. In Figure 5.8, the image of adjusted sampling rate is shown.

The phenomenon of propagation loss may occur anywhere. For example, in case of submarine communications in the Very Low Frequency (VLF), large mountains or valleys would be nasty obstacles. On the other hand, in case of wireless LAN in the Ultra High Frequency (UHF) or the Super High Frequency (SHF), even a tiny gadget on a desk would be a troublesome obstacle.

Chapter 6

Modified Algorithm for Discretizing RRS

6.1 Introduction

Regardless of the method we use to solve the propagation problem, it is crucial to determine what size we should discretize the RRS profile for the final numerical results. It should be noted that the smaller the discretizing interval becomes, the more computation time we need to obtain accurate solutions. Consequently, we must pay much attention to determine the size of discretizing intervals to solve various kinds of problems related to EM wave propagation along RRSs [28].

In this chapter, we firstly introduce a criterion for discretizing intervals regarding RRSs, considering the relationship between RRS parameters, that is height deviation dv and correlation length cl, and discretizing intervals Δx and Δy. We show numerical examples for 1D and 2D RRSs based on the proposed criterion, and we finally propose a modified algorithm for discretizing RRS.

6.2 Criterion for Discretizing RRS

As we explained in Chapter 2, terrestrial surface is characterized by the height deviation dv and correlation length cl. And the slope is expressed in terms of the two parameters as follows [12]:

$$S_\ell = \sqrt{\frac{dv}{cl}}\,. \tag{6.1}$$

Now we define the interval Δx and Δy for discretizing RRS by multiplying the normalized correlation length by M and dividing it by N as follows:

$$\begin{aligned} \Delta x, \Delta y &= \frac{M\tilde{cl}}{N} \\ \tilde{cl} &= \frac{cl}{\sqrt{1+S_\ell^2}} \end{aligned} \tag{6.2}$$

where $\tilde{cl}$ is the normalized correlation length defined by the second equation of Eq.(6.2). Consequently, N is the number of partitions of the normalized correlation length, and the discretizing intervals Δx and Δy are defined by the normalized correlation length divided by N and multiplied by M.

Fig.6.1 shows a coarse RRS profile with unit multiplication and division, M=20 and N=20, that is $\Delta x = \tilde{cl}$, in comparison with a fine RRS profile with unit multiplication and 20 divisions, M=1 and N=20, that is $\Delta x = \tilde{cl}/20$.

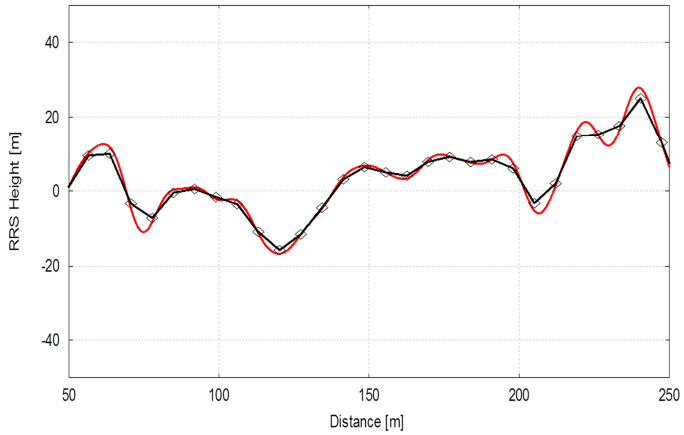

Figure 6.1: Comparison of generated RRS profiles between unit division (N=20, M=20) and 20 divisions (N=20, M=1).

Fig.6.2 shows a little coarse RRS profile with unit multiplication and 5 division, M=4 and N=20, that is $\Delta x = \tilde{cl}/5$, in comparison with the fine RRS profile with M=1 and N=20, that is $\Delta x = \tilde{cl}/20$.

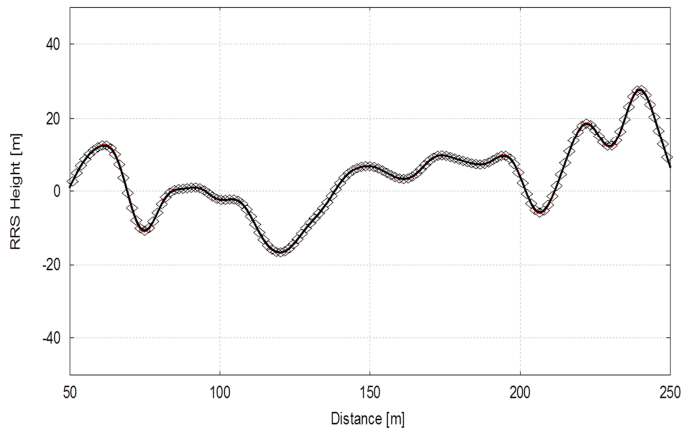

Figure 6.2: Comparison of generated RRS profiles between 5 divisions (N=20, M=4) and 20 divisions (N=20, M=1).

Fig.6.3 shows a less coarse RRS profile with unit multiplication and 10 divisions, M=2 and N=20, that is $\Delta x = \tilde{cl}/10$, in comparison with the fine RRS profile with M=1 and N=20, that is $\Delta x = \tilde{cl}/20$. It is concluded that 5 divisions of the normalized correlation length yield a good accuracy of generated RRS profile. Even if a more better accuracy is required, 10 divisions of the normalized correlation length are enough to get a very fine profile of generated RRS. In these numerical examples, the RRS parameters have been chosen as $dv = 10$ [m] and $cl = 10$ [m].

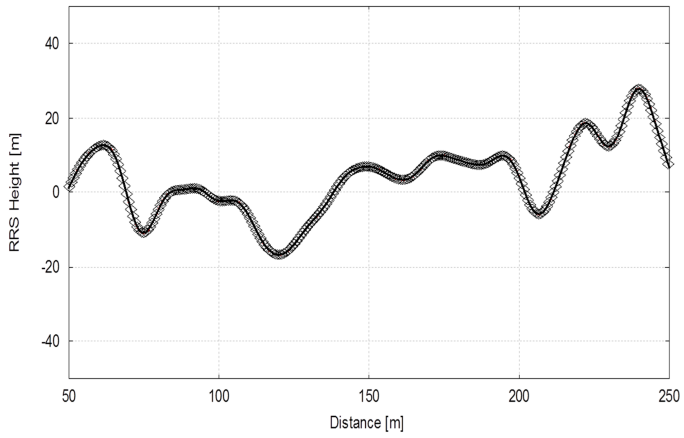

Figure 6.3: Comparison of generated RRS profiles between 10 divisions (N=20, M=2) and 20 divisions (N=20, M=1).

Fig.6.4 shows root mean square errors of coarse RRSs compared with the fine RRS profile with unit multiplication and 20 divisions. The horizontal axis of this figure denotes M/N where M is changed from 2 to 20 with a fixed value of $N = 20$. Numerical results show that the error at $M = 2$ or $M/N = 0.1$ is about 0.1%, and consequently, no error could be observed for $M = 1$ or $M/N = 0.05$. It is shown from this figure that the errors are decreasing almost uniformly when the discretizing interval Δx is decreased. It might be concluded that 20 divisions of the normalized correlation, that is $\Delta x = \tilde{cl}/10$, is enough for us to obtain an excellently smooth RRS for arbitrary dv and cl.

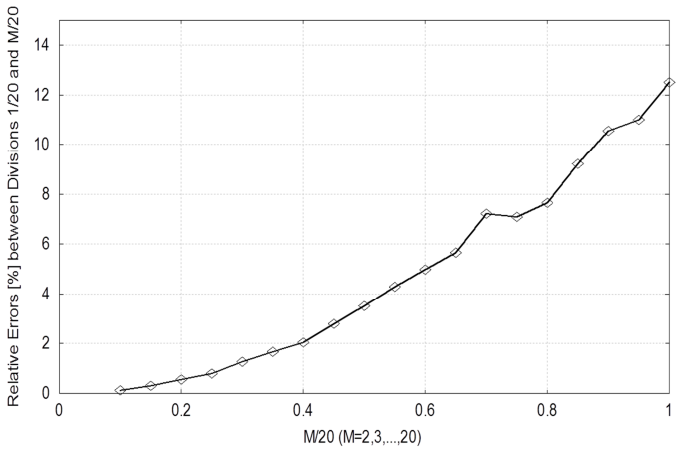

Figure 6.4: Root mean square errors of coarse RRSs ($\Delta x = \tilde{c}lM/20$) in comparison with the fine RRS ($\Delta x = \tilde{c}l/20$) for $M = 2, 3, \cdots, 20$.

Fig.6.5 shows root mean square errors of a little coarse RRS with $\Delta x = 2\tilde{c}l/N$ compared with a RRS with $\Delta x = \tilde{c}l/N$ where the horizontal axis of this figure denotes $2/N$ for $N = 2, 3, \cdots, 20$. These errors can be considered to be a kind of Cauchy sequence that ensures the uniform convergence of arbitrary series. It is shown from this figure that the errors are decreasing uniformly when the value of N is increased or the discretizing interval Δx is decreased. It might also be concluded that 20 divisions of the normalized correlation, that is $\Delta x = \tilde{c}l/10$, is enough for us to obtain an excellently smooth RRS for arbitrary dv and cl. Thus, it is concluded that $\Delta x \leq \tilde{c}l/5$ is required from a view point of RRS generation by the convolution method.

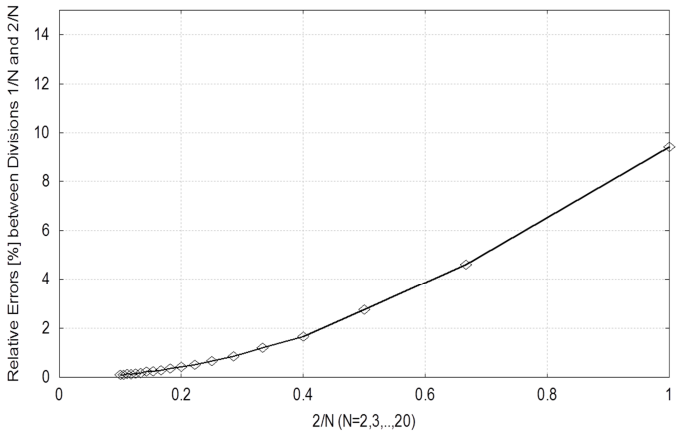

Figure 6.5: Difference of root mean square errors between a little coarse RRSs ($\Delta x = 2\tilde{cl}/N$) and a little fine RRSs ($\Delta x = \tilde{cl}/N$) for $N = 2, 3, \cdots, 20$.

6.3 Numerical Examples Based on the Proposed Criterion

In this section we show some numerical examples obtained by the analytical type of convolution method which follows the criterion for discretizing intervals of the 1D and 2D RRSs as discussed in the preceding sections. Fig.6.6 shows an example of homogeneous 1D RRS with $dv = 5$ [m] and $cl = 10$ [m]. In this case its slope is computed as $S_\ell = \sqrt{3/2}$, and we have employed the criterion for discretizing interval by 5 divisions of the normalized correlation length $\tilde{cl}$, that is $\Delta x = \tilde{cl}/5 = \sqrt{6}$ [m].

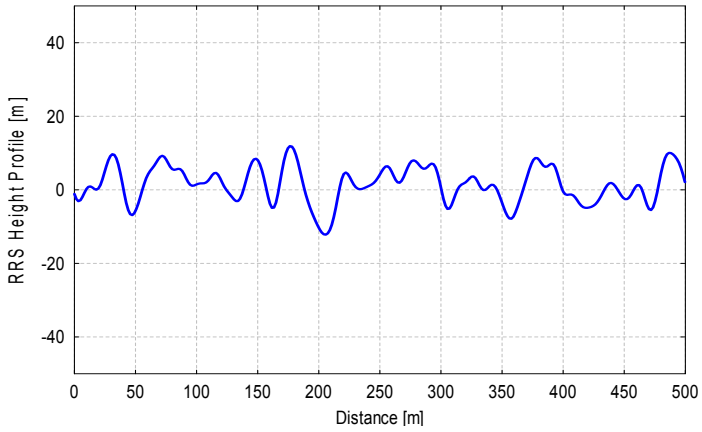

Figure 6.6: An example of generated homogeneous 1D RRS with constant dv and cl.

Fig.6.7 shows an example of inhomogeneous 1D RRS of which correlation length is constant, that is $cl = 10$ [m], but of which standard height deviation is variable as described by

$$dv = 5 + 3\cos(2\pi x/r_s - \pi) \tag{6.3}$$

where $r_s = 500$ [m] is the length of RRS. It is evident that dv becomes maximum at the center of the figure, that is $dv = 8$ [m] at $x = r_s/2 = 250$ [m]. In this case, we have employed the same discretizing interval Δx as the former homogeneous case, because the averaged values of dv is the same as the preceding homogeneous RRS case.

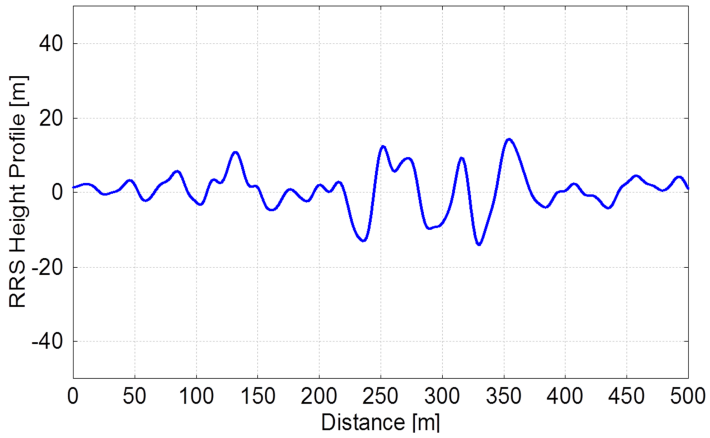

Figure 6.7: An example of generated inhomogeneous 1D RRS with variable dv and constant cl.

Fig.6.8 shows an example of inhomogeneous 1D RRS of which standard height deviation is constant, that is $dv = 5$ [m], but of which correlation length is variable as indicated by

$$cl = 10 + 5\cos(2\pi x/r_s - \pi) \tag{6.4}$$

where $r_s = 500$ [m] is the length of RRS. It is evident that cl becomes maximum at the center of the figure, that is $cl = 15$ [m] at $x = r_s/2 = 250$ [m]. In this example, we have employed the same discretizing interval Δx as the former homogeneous case, because the averaged values of cl is the same as the former homogeneous RRS case.

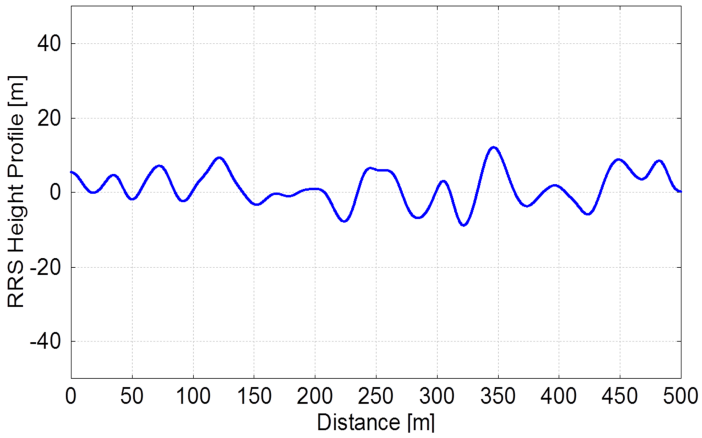

Figure 6.8: An example of generated inhomogeneous 1D RRS with constant dv and variable cl.

Fig.6.9 shows an example of inhomogeneous 1D RRS of which standard height deviation and correlation length are both variable as denoted by

$$\begin{aligned} dv &= 5 + 3\cos(2\pi x/r_s - \pi) \\ cl &= 10 + 5\cos(2\pi x/r_s - \pi) \end{aligned} \tag{6.5}$$

where $r_s = 500$ [m] is the length of RRS. It is evident that both dv and cl become maximum at the center of the figure, that is $dv = 8$ [m] and $cl = 15$ [m] at $x = r_s/2 = 250$ [m]. In this numerical example, we have employed the same discretizing interval Δx as the former homogeneous case, because the averaged values of dv and cl are the same as the preceding homogeneous RRS case.

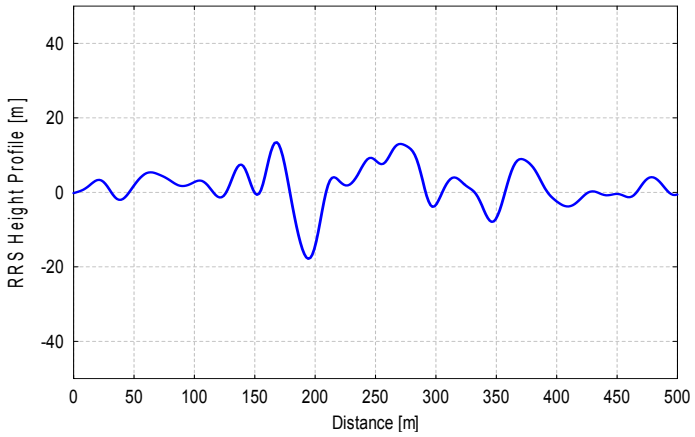

Figure 6.9: An example of generated inhomogeneous 1D RRS with variable dv and variablecl.

Fig.6.10 shows an example of homogeneous 2D RRS with parameters $dv = 5$ [m] and $cl = 10$ [m]. In this case its slope is computed as $S_\ell = \sqrt{3/2}$, and we have employed the criterion for discretizing interval with 5 divisions of the normalized correlation length $\tilde{cl}$, that is $\Delta x = \Delta y = \tilde{cl}/5 = \sqrt{6}$ [m].

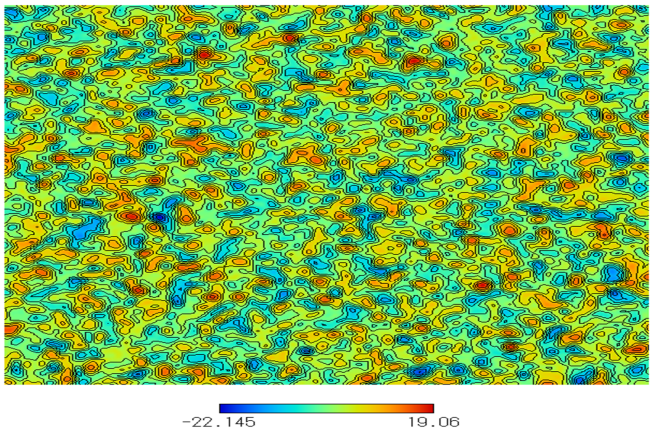

Figure 6.10: An example of generated homogeneous 2D RRS with constant dv and constant cl.

Fig.6.11 shows an example of inhomogeneous RRS of which correlation length is constant, that is $cl = 10$ [m], but of which standard height deviation is variable as described by

$$dv = 5 + 3\cos(2\pi r/r_s) \tag{6.6}$$

where r is the distance from the center of RRS and $r_s = 400$ [m] is the length of RRS in x or y direction. It is evident that dv becomes maximum at the center of the figure, that is $dv = 8$ [m] at $r = 0$. The same value of discretizing intervals Δx and Δy have been used for the present 2D RRS due to the same reason in the former 1D RRS case.

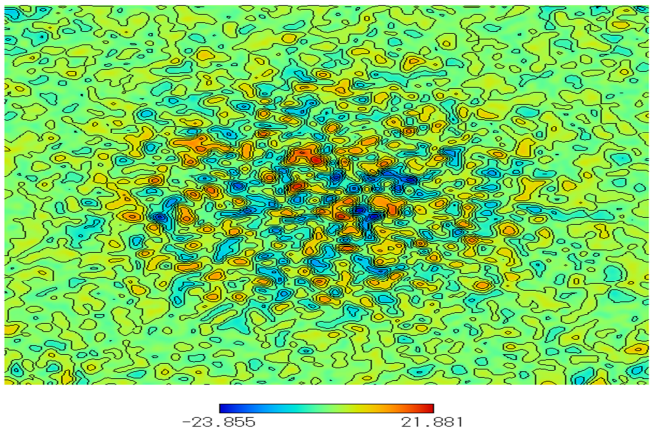

Figure 6.11: An example of generated inhomogeneous 2D RRS with variable dv and constant cl.

Fig.6.12 shows an example of inhomogeneous RRS of which standard height deviation is constant, taht is $dv = 5$ [m], but of which correlation length cl is variable as indicated by

$$cl = 10 + 5\cos(2\pi r/r_s) \tag{6.7}$$

where r is the distance from the center of RRS and $r_s = 400$ [m] is the length of RRS in x or y direction. It is evident that cl becomes maximum at the center of the figure, that is $cl = 15$ [m] at $r = 0$. The same value of discretizing intervals Δx and Δy have been used for the present 2D RRS due to the same reason in the former 1D RRS case.

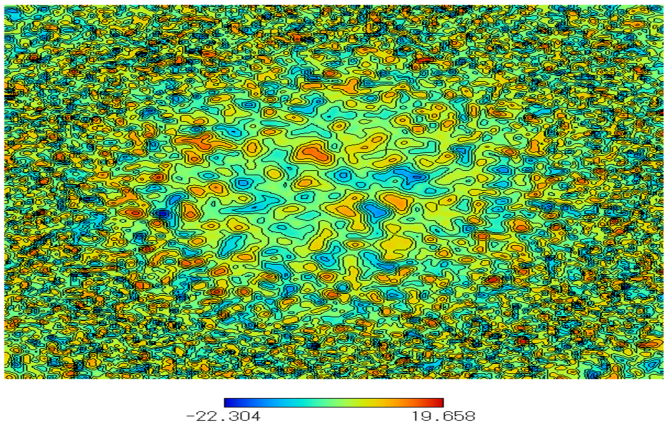

Figure 6.12: An example of generated inhomogeneous 2D RRS with constant dv and variable cl.

Fig.6.13 shows an example of inhomogeneous RRS of which parameters are governed by

$$\begin{aligned} dv &= 5 + 3\cos(2\pi r/r_s) \\ cl &= 10 + 5\cos(2\pi r/r_s) \end{aligned} \tag{6.8}$$

where r is the distance from the center of RRS and $r_s = 400$ [m] is the length of RRS in x or y direction. It is evident that both dv and cl become maximum at the center of the figure, that is $dv = 8$ [m] and $cl = 15$ [m] at $r = 0$. The same value of discretizing intervals have been used for the present 2D RRS due to the same reason as the former 1D RRS case.

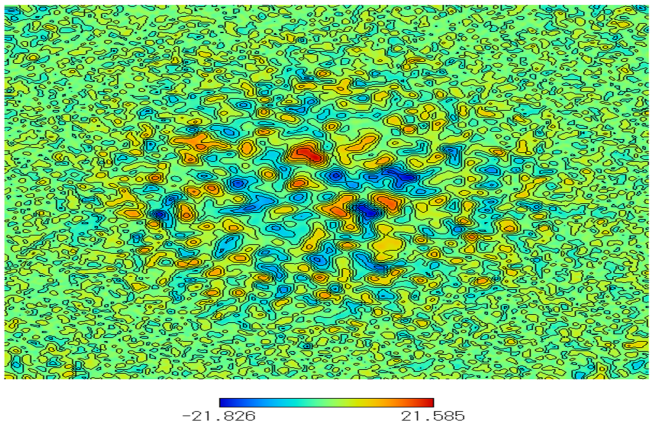

Figure 6.13: An example of generated inhomogeneous 2D RRS with variable dv and variable cl.

6.4 How to Modify the Algorithm

To obtain an accurate profile of rough surface, the plate length should be as shorter as possible. Since computation time is inversely proportional to plate length for searching rays, we propose a new algorithm by modifying the procedure. We regard the flat portion of rough surface as a single-long-plate by connecting its neighboring plates, and we intensely descritize the rough part where diffraction is likely to occur, into multi-short-plates with the length as same as wave length [3].

The new proposed method discretizes terrain profiles dynamically and it can save the computation time for searching rays [29]. This new method is very simple but useful because the estimation is carried out by a simple algorithm keeping accuracy of the profile. And the algorithm is based on the inner product angle between neighbor plates. The relation based on the inner product is given by

$$cos\theta = \frac{\rho_i \cdot \rho_{i+1}}{|\rho_i||\rho_{i+1}|} \quad (i = 0, 1, 2, \cdots, n_{max}) \tag{6.9}$$

where the ρ_i and ρ_{i+1} indicate the position vectors of adjacent plates given by Eq.(2.10). Our study results explain that repeating this equation several times is enough to get a good assessment for the accuracy of this estimation, keeping the shapes of RRS unchanged as well as reducing the number of plates [29].

By using this procedure, adjacent plates are connected and merged into one plate when an inner product angle θ is less than given value θ_m. In the end of this section, we describe the maximum values of θ_m. Figure 6.14 shows a comparison of RRS generated by the proposed method with that of conventional one. The number of plate in the conventional method is 200, and that in the proposed method is 173. It is shown that the shape of RRS does not change even if the number of plates decreases.

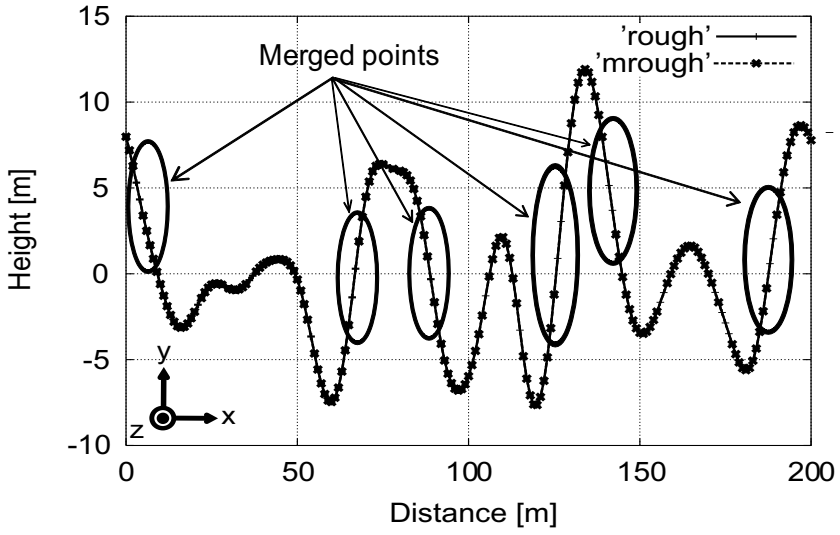

Figure 6.14: Comparison of conventional and proposed RRSs.

When we treat the long distance with large number of plates or RRS which has many flat portions, the effectiveness of proposed method becomes better. As described in chapter 2, discretized plate length in x-axis direction is determined by Eq.(2.11). However, the accuracy of electromagnetic field depends on the discretized plate length. As we explain in section 6.1, we determine that the discretized plate length $\triangle l$ is given by using the RRS parameters. The values of $\triangle l$ are determined by

$$\triangle l = \frac{cl}{N\sqrt{1+{S_l}^2}} \tag{6.10}$$

where the RRS slope S_l is given by

$$S_l = \sqrt{\frac{dv}{cl}}\ . \tag{6.11}$$

We need to select the values of N to be more than 10 which maintains the numerical accuracy as well as the RRS structure.The values of $\triangle l$ should be also larger than the wavelength λ to remain the numerical accuracy.

If we select the values computed by the above equation, we can treat the RRSs with the minimum number of plates. In that case, the computed surface remains the RRS shape. We can also remain the numerical accuracy of electromagnetic field as long as we select the inner product angle become within $\theta_m = 0.3^\circ$. We also denote this issue in chapter 7.

6.5 Conclusion

In this chapter, we have discussed the reduction method of computation time using DRTM from two numerical view points, ray searching and field computation. First, we have reviewed the criterion for discretizing RRS along 1D RRSs and 2D RRSs. Second, we have shown some numerical examples based on the proposed criterion, finally we have proposed a modified algorithm for discretizing RRS to reduce the number of discretized plates. The algorithm consequently leads to reduce computation time of ray searching between source and receiver. We have also used the approximation of Fresnel function in order to reduce the field computation time [31].

Chapter 7

Numerical Results

7.1 Introduction

We show some numerical examples of electric field intensities along RRS and compare the results obtained by the proposed method with that of conventional one. We discuss how much computation time is reduced and how much ray searching time is occupied in the RTM computation.

7.2 Numerical Results

Figure 7.1 shows a comparison of RRSs. Three RRSs are shown in this figure: first one shown in Rough line is generated by the conventional convolution method, second one shown in Modify01 line is generated by the proposed method with $\theta_m = 0.1^\circ$ given by Eq.(6.9), and third one shown in Modify03 line is generated by the proposed method with $\theta_m = 0.3^\circ$ also given by Eq.(6.9). The plate number of these cases are 2001, 895 and 280, respectively. It is demonstrated that two accumulated RRSs are in good agreement with original one even if the number of plates becomes fewer.

Next we show numerical results of electric field intensity along RRS. As shown in Fig.7.1, the transmitter is placed at x=0 and its height is settled at $0.5[m]$ just above the rough surface. The receiver is also at $0.5[m]$ high above the rough surface and it is movable along it. It is assumed that the RRS is made of lossy dielectric of which electric property is described by two parameters, dielectric constant ε_r and conductivity σ. In this paper, we assume RRS to be dry soil with $\varepsilon_r = 5.0$ and $\sigma = 0.0023[S/m]$ [30]. We also select parameters as follows: frequency $f = 1.0GHz$, input power $P = 1[W]$.

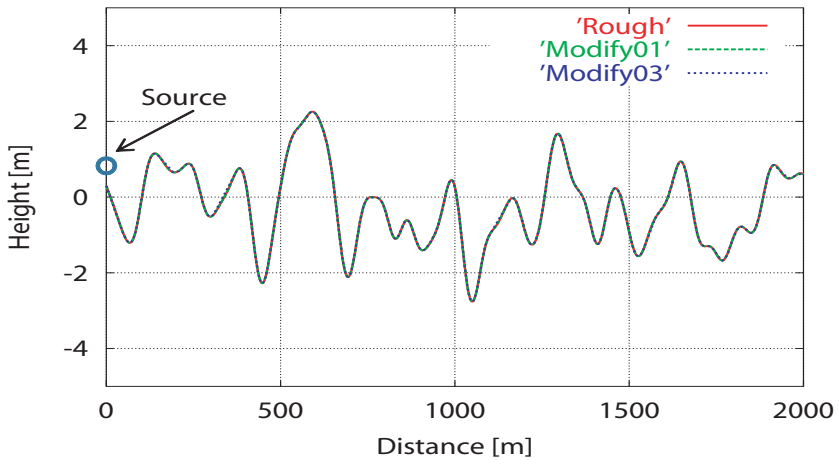

Figure 7.1: Comparison of RRSs.

We have employed the proposed method and the approximation of Fresnel function for reducing ray searching time and field computation time respectively. The approximation of Fresnel function was proposed by the authors, and the accuracy was already demonstrated by comparing it with the rigorous solution [31].

Figure 7.2 shows field intensity distributions along RRS for cl=50m and dv=1m with five different inner product angle and we select the inner product angle $\theta_m = 0°$, $0.01°$, $0.05°$, $0.1°$ and $0.3°$. Although the accuracy becomes worse when the value of θ_m becomes large, the correctness is approximately the same as the conventional one when $\theta_m = 0.01°$ and $0.05°$. And the computation times in sec for each of these five cases are about 880, 710, 400, 140 and 8, respectively, it is reduced about 80 % with $\theta_m = 0.01°$and 40 % with $0.05°$. As a result, it is found that the proposed approximation is useful for reducing the DRTM computation time by selecting the inner product angle within a certain number of the value.

We show other numerical examples. Figure 7.3 shows field intensity distributions along RRS for cl=50m and dv=5m and Figure 7.4 shows them for cl=30m and dv=1m. And Figure 7.5 shows them for cl=100m and dv=1m. From these numerical results, we have found that the accuracy remains better even if the θ_m in Eq.(6.9) becomes a certain large degree within $0.3°$, and the computation time is much saved even if there are many NLOS regions in the field. Figure.7.4 depicts the case as correlation length cl is rather small.

We show computation time of ray searching and field calculation in Table 7.1. The ray searching time occupies about 97% in the total computation time. We have found that

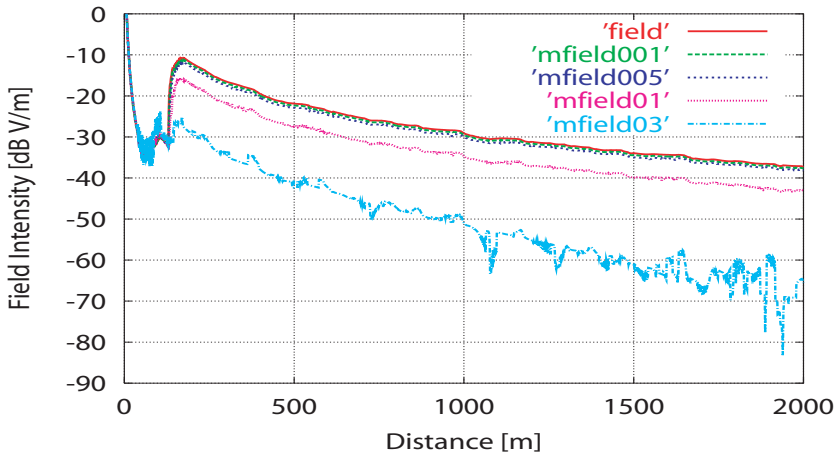

Figure 7.2: Field intensity distribution along RRS with cl=50m and dv=1m.

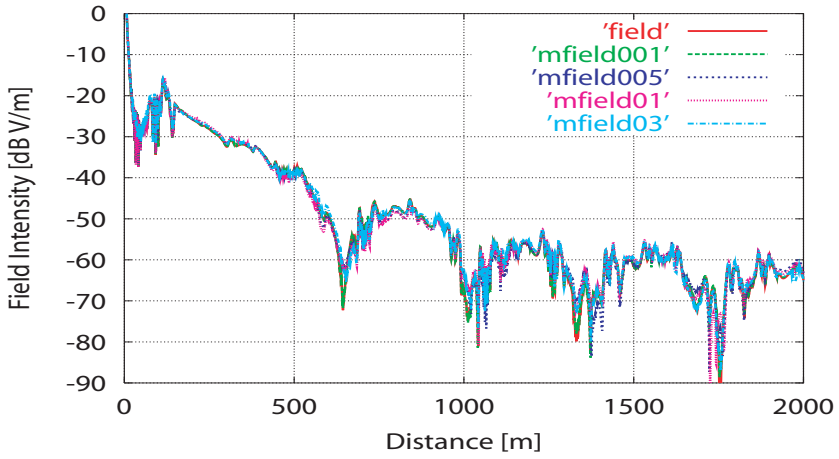

Figure 7.3: Field intensity distribution along RRS with cl=50m and dv=5m.

these inner product values satisfied with the numerical results obtained by Eq.(6.10). In the numerical computation, we have used the computer at Fukuoka Institute of Technology to obtain these results, and the specification of which is AMD Opteron dual processor 8218, clock frequency 2.6 [GHz], 4 CPU (8 way) and 20 [GB] memory.

In this chapter, we have discussed the electromagnetic waves along only 2D RRSs. However, the proposed method can be applied to three dimensional (3D) cases. In case of 3D RRS, its profile is discretized by triangular or approximated rectangular faces [32]. Of cause, the DRTM in 3D requires more computer memory and computation time than 2D cases. Similarly, we can reduce much computation time in 3D analysis by using the

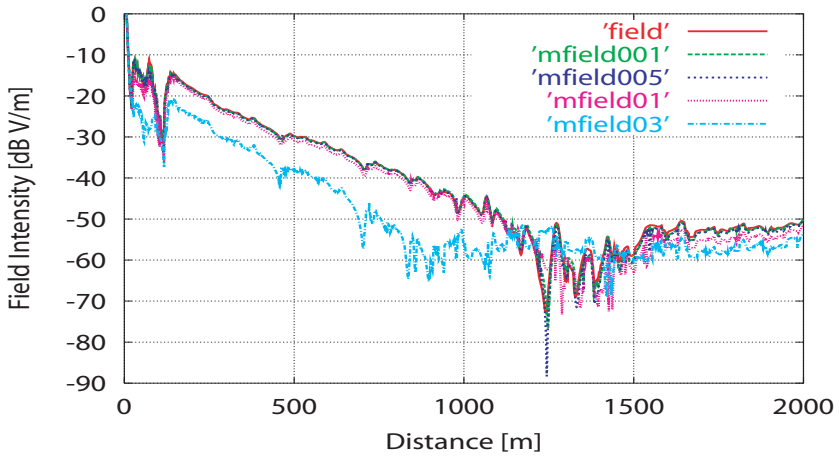

Figure 7.4: Field intensity distribution along RRS with cl=30m and dv=1m.

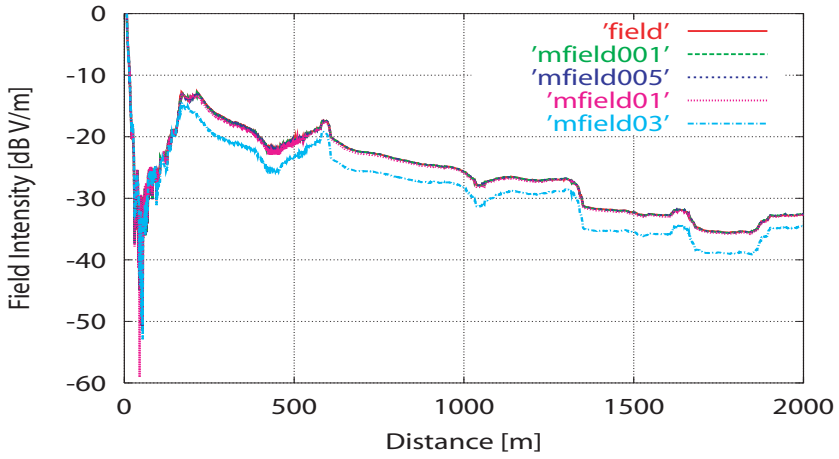

Figure 7.5: Field intensity distribution along RRS with cl=100m and dv=1m.

proposed algorithm which employs the position vector consisting the discretized faces and the normal vector.

7.3 Conclusion

In this chapter, we have shown some numerical results from the modified algorithm. By applying proposed methods, we have saved much computation time, and the accuracy is good in comparison with the conventional numerical results.

Table 7.1: Computation time of ray searching and field computation.

RRS parameters	θ (inner product)	Number of plates	computation time [sec]		Reduction rate [%]		Accuracy
			Ray searching	Field calculation			
cl=30 [m] dv=1 [m]	0 (conventional)	2000	430.34		100		○
			419.18	11.16	100	100	
	0.01	1924	403.50		93.76		○
			394.06	9.44	94.01	84.59	
	0.05	1698	312.11		72.53		○
			303.76	8.35	72.47	74.82	
	0.1	1481	239.88		55.74		○
			233.35	6.53	55.67	58.51	
	0.3	790	46.74		10.86		×
			44.67	2.07	10.66	18.55	
cl=50 [m] dv=1 [m]	0 (conventional)	2000	881.78		100		○
			851.63	30.15	100	100	
	0.01	1834	708.52		80.35		○
			687.64	20.88	80.74	69.25	
	0.05	1349	398.59		45.20		○
			385.09	13.50	45.22	44.78	
	0.1	894	139.17		15.78		×
			133.32	5.85	15.65	19.40	
	0.3	279	7.79		0.88		×
			7.19	0.6	0.84	1.99	
cl=50 [m] dv=5 [m]	0 (conventional)	2000	830.79		100		○
			799.55	31.24	100	100	
	0.01	1961	807.57		97.21		○
			783.32	24.25	97.97	77.62	
	0.05	1830	649.23		78.15		○
			628.83	20.40	78.65	65.30	
	0.1	1693	552.23		66.47		○
			537.81	17.42	67.26	55.76	
	0.3	1231	309.67		37.27		○
			298.66	11.01	37.35	35.24	
cl=100 [m] dv=1 [m]	0 (conventional)	2000	629.92		100		○
			592.77	37.15	100	100	
	0.01	1981	613.35		97.37		○
			583.85	29.50	92.68	79.41	
	0.05	1905	569.10		90.34		○
			541.68	27.42	85.99	73.81	
	0.1	1814	502.06		79.70		○
			477.15	24.91	80.49	67.05	
	0.3	1480	311.57		49.46		×
			295.69	15.88	49.88	42.75	

Chapter 8

Concluding Remarks

8.1 Conclusions

In this thesis, the author proposes a new method to reduce field computation time by adding a new algorithm to DRTM propagation analysis. The author's team introduced a criterion for discretizing intervals and implemented the new algorithm and investigated its performance in different kinds of propagation environments.

Chapter 1 presents an introduction to this thesis, describing the background, purpose and contributions of the research and its outline.

Chapter 2 reviews the principles of the DRTM and introduces field computation to describe its theory, the discretization of rough surfaces, and ray tracing.

- Various kinds of RRSs are examined when analyzing different kinds of propagation environments for DRTM analysis.
- The chapter first describes a convolution method that numerically generates many kinds of RRSs characterised by two parameters: a correlation length (cl) and a height deviation (dv).
- The chapter then discusses the principles of the discretization of rough surfaces and ray tracing.
- The chapter finally touches upon the theory of field computation.

The essence of the DRTM is to discretize not only RRSs but also ray tracing. The former helps saving computer memory, and the latter simplifies the ray searching algorithm, which results in saving computation time.

Chapter 3 evaluates the DRTM to check its accuracy, focussing on accurate numbers of plates discretizing the cylinder's surfaces.

- The chapter evaluates the DRTM, applying the source and image diffraction coefficients to the EM scattering by a cylindrical conductor to check the accuracy of the DRTM. The evaluation is made in comparison with rigorous analytical solutions.
- The chapter also evaluates the DRTM with plane wave diffraction by a conducting half-plane since scattered fields for this problem can be computed rigorously by using the Fresnel function.
- Numerical examples are shown for the source and image diffraction rays as well as field distributions.
- The chapter discusses the accuracy of the DRTM in comparison with the rigorous solutions, focussing on the number of plates discretizing the cylinder.
- The chapter demonstrates that the DRTM has accurate field computation. There actually exists an appropriate, optimal number for the cylinder discretization.

Chapter 4 refers to related work on field estimation for long distance propagation problem. The application of the DRTM to a long distance and its results are described in this chapter.

- The author imported terrain profile data by using the GIS to apply the DRTM to the analysis of long distance propagation.
- The author's team have carried out numerical simulations for electric field distributions from the main station at Fukuoka Tower as well as from the relay stations at Mt. Kaya and in the Fukae area.
- The results of the simulations demonstrate that blind zones of the main station are clearly and effectively cancelled by relay stations located at appropriate positions.

- The results also show that another relay station with small input power is required if the above- mentioned relay stations can not cover all the blind zones thoroughly.

Thus it can be concluded that the DRTM is significantly useful in solving long-distance propagation problems and deciding where to allocate relay stations efficiently.

Chapter 5 discusses diffracted edge points and their sampling rates. It explains intense sampling rates are needed in the edge points and less intense sampling rates in the plain areas.

- Excessive discretization causes propagation loss in shadow regions because of a lack of sampling points especially at the mountain summits.
- The author proposes to set the parameters of the discretization rates arbitrarily depending on locations: for example, more sampling points at mountain summits and fewer in the plain areas.
- With these settings, the author posits that the accuracy of the simulation results will be better and the computation time will be shorten. In Figure 5.8, the image of adjusting sampling points is shown.

Chapter 6 presents the author's proposal of a modified algorithm and explains how valuable plate lengths for various land profiles can reduce computation time for ray searching.

- The chapter reviews the conventional criterion for discretizing RRSs along 1D RRSs and 2D RRSs.
- The chapter shows some numerical examples based on the author's proposed criterion.
- The author implemented his new, modified algorithm for RRS discretization to reduce the number of discretized plates.
- The chapter shows that the proposed algorithm consequently reduces the computation time of ray searching between the source and receiver.
- The approximation of the Fresnel function is also used to reduce the calculation time.

- The proposed method saves much computation time, and the accuracy is sufficiently kept in tact in comparison with the results of the conventional numerical methods.

In Chapter 7, the author discusses the numerical results of the modified algorithm and evaluates the new method.

- The chapter shows some numerical results of the modified algorithm.
- The proposed method saves much computation time, and the accuracy is sufficiently good in comparison with the results of the conventional numerical methods.
- The proposed method needs to select certain values of the inner product angle to maintain the accuracy of field intensity.
- The inner product angle θ_m is a logical choice to deal with RRS slopes as the values of θ_m turn out to be within approximately 0.3° at the most.
- The percentage of ray searching time accounts for the total computation time.

Chapter 8 concludes the thesis and discusses the future work of this research.

8.2 Future Work

The proposed method saves much computation time, and the accuracy is satisfactory in comparison with the results of the conventional numerical method. However, the new method needs to select certain values of the inner product angle θ_m to maintain the accuracy of field intensity. The inner product angle θ_m is a logical choice to deal with RRS slopes as the values come within approximately 0.3° at the most.

To use the new method for a 3D analysis with the GIS system, the method needs to be improved further so that it can be used for sensor-node allocation and for designing and constructing various kinds of radio network links in both open and closed areas. These will be our future research.

References

[1] R. James, “The Ancient and Modern History of EM Ground-Waves Propagation," *IEEE Antennas and Prop.*, Vol. 40, No. 5, Oct. 1998.

[2] Ministry of Internal Affairs and Communications, Japan. Information and Communications (2010) ‘White Paper,’ Available: http://www.soumu.go.jp/johotsusintokei/whitepaper/eng/WP2010/2010-index.html. *White Paper.*

[3] J. Honda, K. Uchida and M. Takematsu (2011) ‘Field estimation for terrestrial digital broadcasting in Western part of Fukuoka,’ Int. J. Space-Based and Situated Computing, Vol. 1, Nos. 2/3, pp. 189-196.

[4] H. Shimizu, H. Matsui, M. Ishii, K. Sakawa, T. Kobayashi,“LOS and NLOS Path-Loss and Delay Characteristics at 3.35 GHz in a Residential Environment," *IEICE Trans. Fundamentals*, Vol. E83-A, No. 7, July. 2000.

[5] H. Harada, T. Yamamura, Y. Kamio, M. Fujise, “Adaptive Modulated OFDM Radio Transmission Scheme Using a New Channel Estimation Method for Future Broadband Mobile Communication Systems," *IEICE Trans. Commun.,* Vol. E85-B, No. 12, Dec. 2002.

[6] K. Uchida, H. Fujii, M. Nakagawa, X.F. Li and H. Maeda ‘FVTD Analysis of Electromagnetic Wave Propagation along Rough Surface’, IEICE Trans. Commun., Vol. J90-B, No. 1, pp. 48-55, June. 2007.

[7] K.Y. Yoon, M. Tateiba and K. Uchida,“FVTD Simulation for Random Rough Dielectric Surface Scattering at Low Grazing Angle," *IECE Trans. Electron.,* Vol. E83-C, No.12, pp. 1836-1843, Dec. 2000.

[8] J. Honda and K. Uchida 'Discrete Ray-Tracing Method (DRTM) Analysis of Propagation Characteristics along Random Rough Surface in Relation to Development of Wireless Sensor Network', Proceedings of The 2009 IEEE Radio and Wireless Symposium, TU2P-4, pp. 248-251, Jan. 2009.

[9] J. Honda and K. Uchida 'FVTD Analysis of Propagation Characteristics in Relation to Random Rough Surface Spectrum', Proceedings of ISAP 2008, pp. 1346-1349, Oct. 2008.

[10] J. Honda, K. Uchida and K.Y. Yoon,"Estimation of Radio Communication Distance along Random Rough Surface", *IEICE Trans. ELECTRON.*, Vol. E93-C, No. 1, pp. 39-45, Jan. 2010.

[11] K. Uchida and J. Honda "Estimation on Radio Communication Distance and Propagation Characteristics along Random Rough Surface for Sensor Networks, Wireless Sensor Networks": *Application-Centric Design, Geoff V Merret and Yen Kheng Tan (Ed.), InTech,* Chapter 13, pp. 231-248, Dec. 2010.

[12] E.I. Thoros, "The validity of the Kirchhoff approximation for rough surface scattering using a Gaussian roughness spectrum," *J. Acoust. Soc. Am.,* Vol. 83, No. 1, pp. 78-92, Jan. 1988.

[13] K. Uchida, J. Honda and K.Y. Yoon: "An Algorithm for Rough Surface Generation with Inhomogeneous Parameters", Journal of Algorithms & Computational Technology, Vol. 5, No. 2, pp.259-271, Mar. 2011.

[14] K. Uchida, M. Takematsu, J.H. Lee, K. Shigetomi and J. Honda: "An Analytic Procedure to Generate Inhomogeneous Random Rough Surface", NBiS 2013, Gwangju, Korea, pp.494-501, Sep. 2013.

[15] G.R. Valenzuela, J.W. Wright and J.C. Leader, "Comments on 'The relationship between the Kirchhoff approach and small perturbation analysis in rough surface scattering theory'," *IEEE Trans. Antennas Propag.*, Vol. AP-20, No. 4, pp. 536-539, July 1972.

[16] J.S. Chen and A. Ishimaru, "Numerical simulation of the second-order Kirchhoff approximation from very rough surfaces and a study of backscattering enhancement," *J. Acoust. Soc. Am.,* Vol. 88 (4), pp. 1846-1850, Oct. 1990.

[17] E.I. Thoros, “The validity of the perturbation approximation for rough surface scattering using a Gaussian roughness spectrum," *J. Acoust. Soc. Am.,* Vol. 86, No. 1, pp. 261-277, July 1988.

[18] D. Holiday, L. L. DeRead, Jr., and G. J. St-Cyr, “New equations for electromagnetic scattering by small perturbations of a perfectly conducting surface," *IEEE Trans. Antennas Propag.,* Vol. 46, No. 10, pp. 1427-1432, Oct. 1998.

[19] V. I. Tatarskii and V. V. Tatarskii, “Statistical description of rough-surface scattering using the quasi-small-slope approximation for random surfaces with a Gaussian multivariate probability distribution," *Waves in Random Media*, Vol. 4, pp. 191-214, 1994.

[20] E. I. Thoros and S. L. Broschat, “An investigation of the small slope approximation for scattering from rough surfaces. Part II. Numerical studies," *J. Acoust. Soc. Am.,* Vol. 101, No. 5, pp. 2615-2625, May. 1997.

[21] M. Takematsu, K. Uchida, J. Honda, “Relation between Discrete Points of DRTM and Diffraction Points," *Proc. The 2012 Seventh Int’l Conf. on Broadband, Wireless Computing, Communication and Applications*, pp.482-487, Nov. 2012.

[22] R.E. Collin, “Antennas and Radio Wave Propagation," *McGraw-Hill Inc.,* New York, pp.13-86, 1985.

[23] B. Noble,“Methods based on the Wiener-Hopf technique," *Pergamon Press*, 1958.

[24] P.M. Morse and H. Feshbach, "Methods of Theoretical Physics," *McGraw-Hill Book Co. Inc.,* Chapter 11 - The wave equation, pp.1331-1583, 1958.

[25] K. Uchida, J. Honda and K. Y. Yoon,“Approximate solution to wedge diffraction for discrete ray tracing method," *Proc. KJJC-AP/EMC/EMT 2009,* pp.303-306, May. 2009.

[26] J. Takada, "Basic Theory of Radio Wave Propagation," Available: http://www.apmc-mwe.org/mwe2005/src/TL/TL05-01.pdf (2005).

[27] M. Takematsu, K. Uchida and J. Honda:"Investigation of observational plate length and diffraction point for DRTM", Int. J. Space-Based and Situated Computing, Vol. 3, No. 4, pp.185-192, Dec. 2013.

[28] M. Takematsu, J. Honda, Y. Kimura and K. Uchida: "Method for Reduction of Field Computation Time for Discrete Ray Tracing Method", IEICE Trans. Electron., vol.E97-C , no.3, pp.198-206, Mar. 2014.

[29] Y. Kimura, J. Honda, M. Takematsu and K. Uchida, “On Reduction of Computation Time of Discrete Ray Tracing Method," *ITE Technical Report*, Vol. 36, No. 3, BCT2012-8, pp. 29-32, Jan. 2012.

[30] M. Sato, “Subsurface imaging by ground penetrating radar," *IEICE Trans. Electron. (Japanese Edition),* Vol. J85-C, No.7, pp. 520-530, July. 2002.

[31] Y. Kimura, J. Honda and K. Uchida, “Application of Horner Method to Approximate Fresnel Function," *Proc. The IEEE Int’l Conf. on Intelligent Networking and Collaborative System*, pp. 430-433, Fukuoka, Japan, Nov. 2011.

[32] J. Honda and K. Uchida,“Delay spread of electromagnetic waves along random rough surface," *Int.J. Ambient Intelligence and Humanized Computing*, Vol. 4, Issue 3, pp. 339-346, 2013.

List of Abbreviations

RRS - Random Rough Surface
DRTM - Discrete Ray Tracing Method
RTM - Ray Tracing Method
EM - Electro Magnetic
FVTD - Finite Volume Time Domain
PO/GO - Physical Optics and Geometrical Optics
GIS - Geographic Information System
DFT - Discrete Fourier Transformation
LOS - Line Of Sight
NLOS - Non Line Of Sight
VLF - Very Low Frequency
UHF - Ultra High Frequency
SHF - Super High Frequency

List of Papers

Journals Papers

1. J. Honda, K. Uchida and M. Takematsu, “ Field Estimation for Terrestrial Digital Broadcasting in Western Part of Fukuoka ” International Journal of Space-Based and Situated Computing, Vol.1, Nos. 2/3, pp. 189-196, May. 2011.

2. Junichi Honda, Kazunori Uchida, Masafumi Takematsu, "ANALYSIS OF FIELD INTENSITY DISTRIBUTION IN INHOMOGENEOUS PROPAGATION ENVIRONMENT BASED ON TWO-RAY MODEL", Journal of Mobile Multimedia, Vol. 8, No. 2, pp. 88-104, 2012.

3. K. Uchida, M. Takematsu, J.H. Lee and J. Honda:"A particle swarm optimisation algorithm to generate inhomogeneous triangular cells for allocating base stations in urban and suburban areas", Int. J. Space-Based and Situated Computing, Vol. 3, No. 4, pp.207-214, Dec. 2013.

4. Masafumi Takematsu, Kazunori Uchida, Junichi Honda, “ Investigation of Observational Plate Length and Diffraction Point for DRTM ”, International Journal of Space-Based and Situated Computing, Vol.3, No.4, pp.185-192, Dec. 2013.

5. Masafumi Takematsu, Junichi Honda, Yuki Kimura, Kazunori Uchida,“ Method for Reduction of Field Computation Time for Discrete Ray Tracing Method ”, IEICE Transactions on Electronics, Vol. E-97C , No 3. pp. 198-206, Mar. 2014.

International Conference Papers

1. K. Uchida, J. Honda, M. Takematsu and T. Tazume:" Field Estimation for Terrestrial Digital Broadcasting in Fukuoka Area", The 2010 International Workshop on Information Communication Technology at KMITL, Bangkok, Thailand, W4B-4, pp.1-6, Aug. 2010.

2. Kazunori Uchida, Junichi Honda, Masafumi Takematsu, and Toshiaki Tazume: "Field Estimation for Terrestrial Digital Broadcasting in Western Part of Fukuoka",2010 International Conference on Broadband, Wireless Computing, Communication and Applications, pp.633-638, Nov. 2010.

3. K. Uchida, J. Honda, T. Tamaki and M. Takematsu, " Handover Simulation based on a Two-Rays Ground Reflection Model ", Proceedings of The 2011 International Conference on Complex, Intelligent, and Software Intensive Systems, pp. 414-419, June 2011.

4. Masafumi Takematsu, Junichi Honda and Kazunori Uchida:"Electric Field Intensity Computed by DRTM in Relation to the Number of Plate Observation Points and Frequency", Proceedings of the 2011 Third International Conference on Intelligent Networking and Collaborative Systems, pp.412-417, Nov. 2011.

5. Masafumi Takematsu, J. Honda and K. Uchida: " On Accuracy of Didscrete Ray Tracing Method in Comparison with Rigorous Solutions ", Proc. of IEEE AINA-2012, Fukuoka, Japan, pp.633-638, Mar. 2012.

6. K. Uchida, M. Takematsu, J.H. Lee and J. Honda :"An Adaptive Algorithm Based on PSO for Generating Inhomogeneous Triangular Cells", Proceedings of CISIS-2012, Palermo, Italy, pp.654-659, July 2012.

7. Kazunori Uchida, Masafumi Takematsu and Junichi Honda: "An Algorithm to Estimate Propagation Parameters Based on 2-Ray Model", Proceedings of NBiS-2012, Melbourne, pp.556-561, Sep. 2012.

8. Kazunori Uchida, Masafumi Takematsu, Jun-Hyuck Lee, Keisuke Shigetomi and Junichi Honda: "Estimation of Field Distributions in Complicated Propagation Environments Based on 1-Ray and 2-Ray Models", Proceedings of The 9th Asia-Pacific Engineering Research Forum on Microwaves and Electromagnetic Theory, Fukuoka, pp.74-81, Oct. 2012.

9. Kazunori Uchida, Masafumi Takematsu, Jun-hyuck Lee, Junichi Honda:"Field Distributions of 1-Ray Model Using Estimated Propagation Parameters in Comparison with DRTM", 2012 Seventh International Conference on Broadband, Wireless Computing, Communication and Applications, Victoria, pp.488-493, Nov. 2012.

10. Masafumi Takematsu, Kazunori Uchida, Junichi Honda:"Relation between Discrete Points of DRTM and Diffraction Points", 2012 Seventh International Conference on Broadband, Wireless Computing, Communication and Applications, Victoria, pp.482-487, Nov. 2012.

11. Kazunori Uchida, Keisuke Shigetomi, Masafumi Takematsu and Junich Honda:" An Estimation Method for Amplitude Modification Factor Using Floor Area Ratio in Urban Areas", Information Technology Convergence: Security, Robotics, Automations and Communication - Lecture Notes in Electrical Engineering 253, pp.101-109, Springer, ISBN 978-94-007-6995-3, July 2013.

12. Keisuke Shigetomi, Masafumi Takematsu, Kazunori Uchida and Junichi Honda:" Estimation of Path Loss in Urban Areas Based on 1-Ray Model Using Building Coverage and Floor Area Ratios", The 7th International Conference on Complex, Intelligent, and Software Intensive Systems (CISIS 2013), Taichung, pp.213-218, July 2013.

13. Jun-Hyuck Lee, Masafumi Takematsu, Kazunori Uchida and Junichi Honda:" Allocation of Sensor Nodes or Base Stations in Inhomogeneous Propagation Environments", The 7th International Conference on Complex, Intelligent, and Software Intensive Systems (CISIS 2013), Taichung, pp.66-71, July 2013.

14. Kazunori Uchida, Masafumi Takematsu, Jun-Hyuck Lee, Keisuke Shigetomi and Junichi Honda: "An Analytic Procedure to Generate Inhomogeneous Random Rough Surface", The 16th International Conference on Network-Based Information Systems (Proceedings of NBiS-2013), Gwangju, Korea, pp.494-501, Sep. 2013.

15. Masafumi Takematsu, Kazunori Uchida and Junichi Honda: "Investigation of Scattered H-wave Based on DRTM", The 16th International Conference on Network-Based Information Systems (NBiS 2013), Gwangju, Korea, pp.513-517, Sep. 2013.

16. K. Uchida, M. Takematsu, J.H. Lee, K. Shigetomi and J. Honda:"Interpolation of Communication Distance in Urban and Suburban Areas", 2013 International Symposium on Antennas and Propagation (ISAP2013), Nanjing, China, pp.873-876, Oct. 2013.

17. Kazunori Uchida, Masafumi Takematsu and Junichi Honda:"Path Loss Estimation for Analytically Expressed Inhomogeneous Random Rough Surface", 2013 8th In-

ternational Conference on Broadband, Wireless Computing, Communication and Applications (BWCCA 2013), Compiegne, France, pp.414-421. Oct. 2013.

18. Kazunori Uchida, Masafumi Takematsu, Jun-Hyuck Lee and Junichi Honda:"Parameter estimation for propagation along random rough surface by using line of sight data", J Mobile Information Systems DOI 10.3233/MIS-130185, IOS Press, pp.307-319, Nov. 2013.

19. K. Uchida , M. Takematsu and Junichi Honda:"A Discretization Criterion for Generating Random Rough Surface Based on Convolution Method", 2014 Eighth International Conference on Complex, Intelligent and Software Intensive Systems, Birmingham, UK, pp.307-312, July. 2014.

20. Kazunori Uchida, Shinsuke Nogami, Masafumi Takematsu and Junichi Honda:"Tsunami Simulation Based on Dijkstra Algorithm", 2014 International Conference on Network-Based Information Systems, Salerno, Italy, pp.114-119, Sep. 2014.

21. Kazunori Uchida, Naoto Hadano, Masafumi Takematsu and Junichi Honda:"Estimation of Propagation in Urban Areas in Terms of Building Coverage and Floor Area Ratios", 2014 International Conference on Network-Based Information Systems, Salerno, Italy, pp.555-561, Sep. 2014.

22. Kazunori Uchida, Takuma Hashimoto, Masafumi Takematsu and Junichi Honda:"Statistics of Electromagnetic Wave Propagation along Random Rough SurfaceTsunami Simulation Based on Dijkstra Algorithm", 2014 International Conference on Network-Based Information Systems, Salerno, Italy, pp.566-571, Sep. 2014.

Domestic Conference Papers

1. 内田一徳，本田純一，玉木太郎，武末正文，“ 秦の実験式から見た 2 波モデルと伝搬特性 ”，電子情報通信学会技術報告，AP2011-14，pp. 49-54，May. 2011.

2. 武末正文，内田一徳，本田純一，“ GIS 地図情報を用いた DRTM による地上波デジタル波の電波伝搬解析 ”，映像情報メディア学会技術報告書，Vol. 35，No. 3，pp. 89-92，BCT2011-22，Jan. 2011.

3. 木村祐樹，本田純一，武末正文，内田一徳，“ 離散型レイトレース法の計算時間の削減について ”映像情報メディア学会技術報告書，Vol. 36，No. 3，BCT2012-8，pp.29-32，Jan. 2012.

4. 内田一徳，李峻赫，武末正文，本田純一："PSO アルゴリズムに基づく不均質伝搬環境下の基地局配置"，電気学会電磁界理論研究会資料，EMT-12-139, pp.107-112, Nov. 2012.

5. 内田一徳，重富圭亮，武末正文，本田純一："１波及び２波モデルによる複雑系伝搬環境下の電界分布推定"，電気学会電磁界理論研究会資料，EMT-12-140, pp.113-118, Nov. 2012.

6. 内田一徳，橋本卓磨，李峻赫，武末正文："不均質ランダム粗面に関する伝搬損失の推定"，電気学会電磁界理論研究会資料，EMT-13-155, pp.1-6, Nov. 2013.

7. 内田一徳，羽田野尚登，重富圭亮，武末正文："奥村・秦モデルを援用した１波モデルによる市街地伝搬の一推定法"，電気学会電磁界理論研究会資料，EMT-13-125, pp.37-42, Nov. 2013.

8. 羽田野尚登，内田一徳，重富圭亮，武末正文：”建蔽率と容積率分布を考慮した市街地伝搬の一推定法 ”，映像情報メディア学会技術報告，Vol.38, No.5, BCT2014-7, pp.25-28, Jan. 2014.d

9. 橋本卓磨，内田一徳，武末正文：”ランダム粗面に対する電波伝搬特性推定法 ”，映像情報メディア学会技術報告，Vol.38, No.5, BCT2014-10, pp.37-40, Jan. 2014.

10. 内田一徳，武末正文，本田純一：”ランダム粗面生成における離散化設定の基準 ”，映像情報メディア学会技術報告，Vol.38, No.5, BCT2014-26, pp.101-104, Jan. 2014.